Finite Cell Method for functionally graded materials based on V-models and homogenized microstructures

Benjamin Wassermann*[1], Nina Korshunova†[1], Stefan Kollmannsberger‡[2], Ernst Rank§[1,3], and Gershon Elber¶[4]

[1]Chair for Computation in Engineering, Technical University of Munich, Arcisstr. 21, 80333 München, Germany

[2]Chair of Computational Modeling and Simulation, Technical University of Munich, Arcisstr. 21, 80333 München, Germany

[3]Institute for Advanced Study, Technical University of Munich, Lichtenbergstr. 2a, 85748 Garching, Germany

[4]Center for Graphics and Geometric Computing, Technion Israel Institute of Technology, Haifa 3200003, Israel

March 26, 2020

This paper proposes a computational methodology that allows a direct numerical simulation of heterogeneous/functionally graded materials based on V-reps/V-models and the Finite Cell Method (FCM). The FCM is an embedded domain approach that employs higher-order finite elements. The basic idea is to embed a complex geometric model into a fictitious domain that is trivial to mesh. The complexity of the geometry is then recaptured by an adapted precise numerical integration scheme for the elements cut by the boundary. For this, only a robust point inclusion test is required, which can be provided by various Computer-Aided Design (CAD) models. V-rep is a geometric modeling framework that represents the entire volume based on tri-variate B-Splines. Consequently, not only a point inclusion test is provided – but also the possibility to represent and model the interior domain. This allows to apply functionally graded material based on the tri-variate basis functions. These material parameters can then be regained during the simulation with an adapted point inclusion test. The potential of the proposed method especially in the context of additive manufacturing is demonstrated by several numerical examples.

Keywords: Functionally Graded Material, V-Reps, V-Models, Finite Cell Method, Direct Simulation, Additive Manufacturing, Homogenization

Submitted to AMSES – special issue on unfitted finite element methods

*benjamin.wassermann@tum.de, Corresponding Author
†nina.korshunova@tum.de
‡stefan.kollmannsberger@tum.de
§ernst.rank@tum.de
¶gershon@cs.technion.ac.il

Contents

1 Introduction

Functionally graded materials (FGM) are a novel class of advanced materials that offer the possibility to exploit various desired physical properties within one component. This allows to manufacture 'high-performance' and 'multi-functional' artifacts which can resist physical exposures that could not be withstood by a single material [1]. The idea of combining different materials goes back more than 4000 years – the development of the composite bow – and has led to modern carbon fiber reinforced polymers. These composite materials change their material properties step-wise and are consequently prone to delamination. In FGM, on the other hand, material properties vary continuously inside the volume and avoid material interfaces [2]. Specific material properties are achieved by continuous changes in the micro-structures, grain sizes, crystal structure, or composition of different materials such as metal, ceramics, polymers, or biological tissues [3, 4]. Prototypes, especially for micro-structures, can be found in nature, such as in bones, seashells, skin, or wood [5] or obtained using topology optimization [6, 7, 8]. Fields of application are, amongst many others, corrosion resistance of chemically exposed components [9], bone-like lightweight porous medical implants [10], or heat resistance of load-bearing parts such as spacecraft thermal shielding, jet turbine blades, or nuclear reactors [3, 11].

Additive manufacturing (AM) or 3D printing is a generic term for various production techniques in which an object is created by layer-wise material deposition. This allows the fabrication of objects of almost arbitrary shape. AM is the method of choice for the fabrication of FGM, as (i) it allows to resolve very fine structures, (ii) it can manufacture internal structures which could not be created with any other method, and (iii) the layer-wise material deposition gives control over the composition of the processed material, as well as over the grain size [12, 13]. With functionally graded additive manufacturing (FGAM), it is possible to create different single- and multi-material FGM [14]. Single FGAM created specimens consist only of one material that changes its properties due to an adaption of the micro-structure, density, or grain size [15]. As AM allows the creation of free form structures, a single-material FGM can be fabricated with any printable material [16]. Multi-material FGM, which combines two or more materials, has recently been under intensive research [17]. A special focus was placed on metal-metal combinations, see e.g. [4] where steel and titanium-based combinations are investigated. More complex are combinations of materials of a different kind, such as ceramic-metal compositions [18]. However, these compositions might carry the most potential, as the underlying material properties are very distinct.

Before fabrication, the behavior of FGM components usually needs to be analyzed by numerical simulations. To this end, an analysis-suitable geometrical model needs to be provided which is naturally created with computer-aided design (CAD) and then transformed into a mesh. This transition process from CAD to an analysis-suitable mesh is error-prone. Depending on the quality of the model, manual work must be invested to heal the original geometry before mesh generation can be carried out successfully. Furthermore, the most used CAD representations, i.e. boundary representation (B-rep) or solid based procedural models, are not well suited for an accurate description of FGM. B-rep models represent their volume implicitly by the boundary surfaces, which are modeled either with linear primitives (e.g. triangles and quads) or with trimmed spline

patches [19]. Consequently, B-rep models offer no possibility to directly represent a heterogeneous material distribution inside the body. A workaround is to create vector functions that carry the material properties for each point. These functions can be classified into four different categories: (i) geometrically-independent, e.g., in Cartesian coordinates, (ii) distance-based, (iii) blending composition, and (iv) sweeping composition functions (for a detailed explanation refer to [20, 21]). However, except (i), these functions only allow a smooth transition of material properties between the different surfaces, which is not suitable for all material distributions. Geometrically-independent functions, on the other hand, are cumbersome as they are not related to the object itself. CAD systems using solid-based procedural models follow the constructive solid geometry (CSG) idea [22]. Here, models are composed of simple primitives: *spheres, cuboids, cylinders, etc.* and more complex primitives: *sweeps, lofts, extrusions, solid of revolution, etc.*. These primitives are combined with the classical Boolean operations: *union, intersection, difference, negation*, and their derivations: *fillet, chamfer, holes, etc.*. Material properties can then easily be assigned to the respective primitives. Of course, this requires special treatment in regions with overlapping primitives [12]. Furthermore, as primitives are typically provided as implicit functions $F(\boldsymbol{x}) = 0$, they offer, similar to B-rep models, no possibility to further resolve the internal volume. Again, vector functions applied to the primitives are a possible workaround. Another possible geometrical representation offered by spatial decomposition, such as voxelized models. Here, each voxel can carry its material properties. These voxel models mostly originate from CT scans (e.g. of bones) and provide only a coarse approximation while requiring an extensive amount of storage capacity. Nevertheless, voxel-based models have been used to resolve fine micro-structures and quasi-continuous changes of the material properties [23, 24].

Massarwi and Elber [25] recently proposed a novel volumetric representation technique (V-rep) for 3D models, which allow full control over the model's interior. V-reps consist of non-singular trimmed trivariate B-spline patches which can be combined into V-models using the Boolean operations. By extending the dimension of the control points to $\mathbb{R}^{3+s}$, it is possible to assign material properties directly to the model. Potentially critical overlapping regions of the V-model are resolved by trimming the involved patches and creating new trivariate primitives for the respective overlapping volume. Due to their non-singularity trivariate B-splines, V-models are predestined for are subsequent simulation using isogeometric analysis (IGA) [26]. However, as the particular patches do not necessarily coincide at their boundary, special techniques are required to glue them together, e.g. Mortar methods [27, 28].

Apart from the possibility to control the interior of the volume, which can be used to model multi-material FGM, the V-rep framework also offers the possibility to create single-material FGM, such as continuously changing microstructures. Although easy to fabricate with AM, these multiscale structures are critical from a simulation point of view. Due to the complexity of the underlying CAD models, the meshing becomes difficult. Additionally, attempts to resolve the structure sufficiently accurate may result in over-refined meshes – which in turn lead to an additional but unnecessary computational effort. This is where numerical homogenization provides an efficient tool to estimate an overall mechanical behavior of such structures. The basic idea of

homogenization is to define a representative volume element (RVE) which is sufficiently large to represent the overall material behavior in the specific region [29, 30, 31]. In the case of periodic microstructures, a unit cell can be extracted for further material characterization. Periodic Boundary Conditions are then applied at their boundaries, which leads to the best possible estimate of the effective behavior [32, 33] among other possible choices. The resulting material characterization can then be used to simulate a complete structure under complex loading. The computational cost is reduced considerably by 'smearing out' the detailed complex geometrical features of a microstructure and expressing them in terms of the effective behavior. Still, on the microscopic level of the RVE, the structure needs to be fully resolved in a boundary conforming fashion to account for all geometrical details. Here, embedded domain methods offer an elegant and reliable alternative over classical FEA also for non-periodic AM structures [34].

Embedded domain methods, such as the finite cell method (FCM) [35] avoid a tedious and error-prone meshing process by embedding the complex geometrical model into a fictitious domain that can be easily meshed into regular simple elements. These methods are known under different names, e.g. fictitious domain [36, 37, 38], immersed FEM/boundary [39, 40], or Cartesian grid method [41]. The FCM [42], uses besides the embedded domain approach also high-order finite element , deploying hierarchical Legendre, spectral, or B-Spline shape functions [43, 44]. Initially developed for 2D and 3D linear elasticity, it was extended to various fields of applications, such as topology optimization [45, 46], local enrichment for material interfaces [47], elastodynamics and wave propagation [43, 48], and additive manufacturing [49]. Further investigations include efficient integration techniques [50, 51] and homogenization [34]. FCM was successfully applied to various geometrical representations, such as B-rep, CSG [52], voxel domains [53], point clouds [54], and defective, mathematically invalid B-rep models [55].

In this contribution, the FCM is extended such that V-rep models with functionally graded material properties can be simulated directly. The paper is structured as follows: Sections 2.1 and 2.3 provide a brief overview over the FCM and V-reps, respectively. The methodology to directly simulate on V-reps is described in section 3.1. Section 3.2 presents and discusses several numerical examples before conclusions are drawn in section 4.

2 Methods

2.1 Finite cell method

The finite cell method is a higher-order embedded domain method. It offers the possibility to directly simulate complex geometric models without the need for a boundary conforming meshing procedure. Further, it does not compromise the accuracy of the underlying finite element method. While a comprehensive description of the method can be found in [42] for a comprehensive description of the method, the basic concepts are summarized for the sake of completeness. Linear elasticity is considered as a model application for FCM.

2.2 Basic fomulation

In the finite cell method, a physical domain Ω_{phy} is embedded into a fictitious domain Ω_{fict} forming an extended domain $\Omega_{\cup}$, as illustrated in Fig. 1 for two dimensions. The weak form of the equilibrium equation for the extended domain $\Omega_{\cup}$ reads as follows

$$\int_{\Omega_U} [\mathrm{L}\boldsymbol{v}]^T \, \alpha \mathrm{C} \, [\mathrm{L}\boldsymbol{u}] \, \mathrm{d}\Omega_{\cup} = \int_{\Omega_U} \boldsymbol{v}^T \, \alpha \boldsymbol{b} \, \mathrm{d}\Omega_{\cup} + \int_{\Gamma_N} \boldsymbol{v}^T \boldsymbol{t} \, \mathrm{d}\Gamma_N \, , \tag{1}$$

where $\boldsymbol{u}$ is the unknown deflection, $\boldsymbol{v}$ is a test function, L is the kinematic differential operator and C is the constitutive material tensor. The body load and the prescribed tractions on the Neumann boundary Γ_N are denoted by $\boldsymbol{b}$ and $\boldsymbol{t}$, respectively. To resolve the complex domain correctly, an indicator function $\alpha(\boldsymbol{x})$ is introduced which weights the material tensor C

$$\alpha(\boldsymbol{x}) = \begin{cases} 1 & \forall \, \boldsymbol{x} \in \Omega_{phy} \\ 10^{-q} & \forall \, \boldsymbol{x} \in \Omega_{fict} \end{cases} \, . \tag{2}$$

In the limit $q = \infty$, eq. (1) recovers the standard weak form for Ω_{phy}. In a finite element-like discretization, however, it leads to ill-conditioned systems. This can be avoided by choosing a finite q (in practice $q = 6...10$) in combination with a suitable preconditioning and/or orthogonalization of the shape functions [56]. This choice introduces a modeling error [57] but limits the conditioning number of the stiffness matrix. Further improvement on the conditioning can be obtained using preconditioning, orthogonalization of shape functions, and/or the increase of continuity between the cut cells [58].

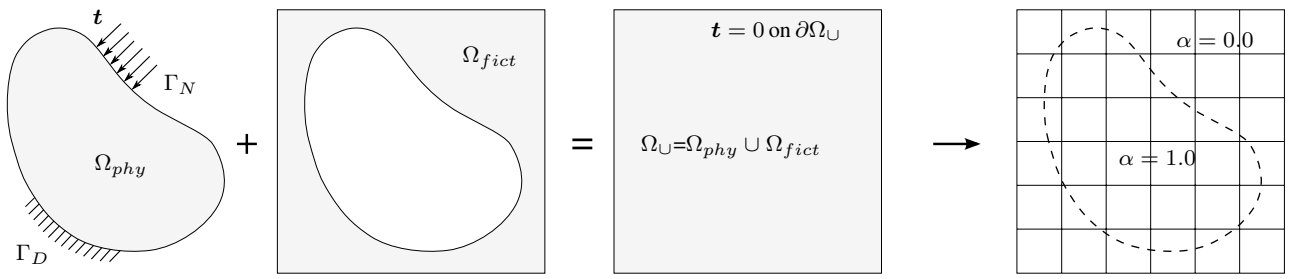

Figure 1: The concept of the finite cell method (taken from [35]).

The extended domain $\Omega_{\cup}$ is of simple shape and can be easily meshed into regular cells, e.g. rectangles in 2D and cuboids in 3D, respectively. These cells can be locally refined into sub-cells or with respect to the order of the shape function [59, 60].

2.2.1 Geometry treatment

The FCM resolves the physical domain Ω_{phy} (i.e. the geometric model) by the discontinuous scalar field $\alpha(\boldsymbol{x})$, which is then queried during the integration of the system matrices and load vectors. Consequently, the resolution of the geometry's complexity is shifted from the discretization (conforming meshing) to the integration

level. The only information the FCM requires from the geometry is an unambiguous point inclusion statement, i.e. it must be possible to decide for any point $\boldsymbol{x}$ whether $\boldsymbol{x} \in \Omega_{phy}$ or $\boldsymbol{x} \in \Omega_{fict}$. Due to the discontinuity of $\alpha(\boldsymbol{x})$ on cut cells, the integration needs to be carried out using special quadrature rules. Common variants are recursive space-tree reconstruction, moment fitting, or smart quadtrees/octrees [61, 62, 63]. Another approach uses dimensional reduction, i.e. the integration is not performed over the entire domain, but only along the boundary [64].

2.2.2 Boundary conditions

As the boundary of the physical domain Ω_{phy} typically does not coincide with the edges/faces of the finite cells, essential (Dirichlet) boundary conditions need to be applied in a weak sense. For this, several methods have been investigated – such as the Nitsche method, Lagrange multipliers, and the penalty method [65, 66, 67, 68]. Natural (Neumann) boundary conditions are applied on Γ_N following Eq. (1). Homogeneous natural boundary conditions are automatically resolved by $\alpha(\boldsymbol{x}) \approx 0$. Inhomogeneous natural and essential boundary conditions require an explicit integrable boundary description, which is either provided by the geometrical model or extracted directly from the volume using, e.g., the marching cubes algorithm, see e.g. [69].

2.3 Volumetric representation

Massarwi and Elber [25] developed a novel geometric modeling technique, based on trimmed volumetric trivariate B-splines, called 'volumetric representation '(V-rep). The interior volume of V-Reps is modeled explicitly and is, thus, able to directly represent functionally graded/heterogeneous material. The V-rep framework provides methods and algorithms for the construction of V-models by combining simple (e.g. cylinder, sphere, etc.) or complex primitives (e.g. ruled primitives or solids of revolution) with the Boolean operations, thus following the idea of Constructive Solid Modeling. Furthermore, it is possible to migrate spline-based B-Rep models to V-Rep models. The V-rep framework is embedded in the Irit geometry library, developed by Elber et al. [70]. Irit provides a vast amount of various geometric modeling and analysis functionalities, and it can be accessed as a C(++) library, via a scripting language, or graphically with the GuIrit CAD environment.

2.4 Trivariate B-splines

A trivariate B-spline is a parametric function that allows to span a volume over a three-dimensional parameter space. It is typically represented as follows

$$\boldsymbol{V}(\boldsymbol{u}) = \sum_{i=1}^{l} \sum_{j=1}^{m} \sum_{k=1}^{n} B_{i,p}(u) B_{j,q}(v) B_{k,r}(w) \boldsymbol{P}_{i,j,k} \,, \tag{3}$$

where $\boldsymbol{V}(\boldsymbol{u})$ is a point inside the volume and $\boldsymbol{u} = (u, v, w)^T$ the corresponding three-dimensional parameter position in the parameter space $\boldsymbol{u} \in U \times V \times W \subseteq \mathbb{R}^3$. $B_{i,p}$ denotes the ith one-dimensional B-spline basis

function of polynomial degree p and $\boldsymbol{P}_{i,j,k} \in \mathbb{R}^k$ are the $l \cdot m \cdot n$ control points. The dimension of the control points is $k = 3 + s$, where $k = 3$ corresponds to the three geometric coordinates $\boldsymbol{x}^T = [x, y, z]$. Further information can be represented by additional dimensions $s > 0$.

2.4.1 V-rep primitives

Apart from the trivial case of a cuboid, the V-rep framework offers a variety of both high-level and simple primitives. Implemented are several high-level primitive constructors, all of which yield one single trivariate patch (see Fig. 2):

1. Extrusion: A surface is extruded along a vector.
2. Ruled solid: A volume is defined as a linear interpolation between two surfaces.
3. Solid of revolution: A volume is constructed by rotating a surface around an axis.
4. Boolean sum: A volume is created from six boundary surfaces [71].
5. Sweep/Loft: A sweep or loft interpolates several surfaces along a sweeping path.

Simple primitives – such as spheres, cylinders, tori, and cones – can not be represented by a single trivariate patch without introducing singularities (e.g. at the mid axis of a sphere, the Jacobi matrix vanishes $\det(J_{\boldsymbol{V}}(r = 0)) = 0$.) To this end, singular primitives are composed of several non-singular trivariate patches (see Fig. 3).

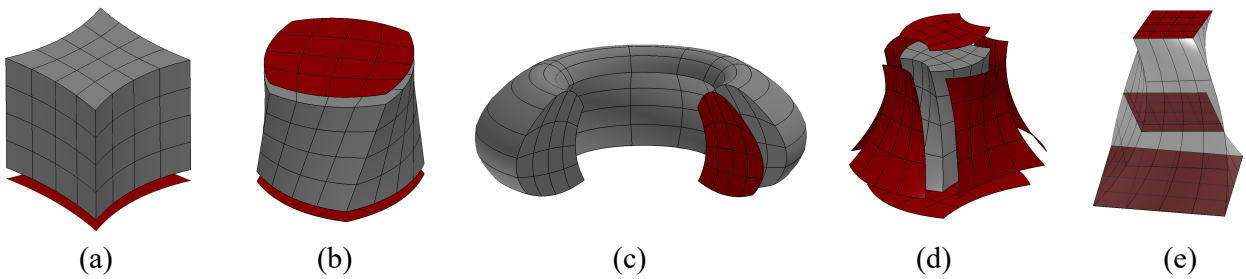

Figure 2: High-level primitives: (a) extrusion, (b) ruled solid, (c) volume of revolution, (d) boolean sum, and (e) sweep/loft.

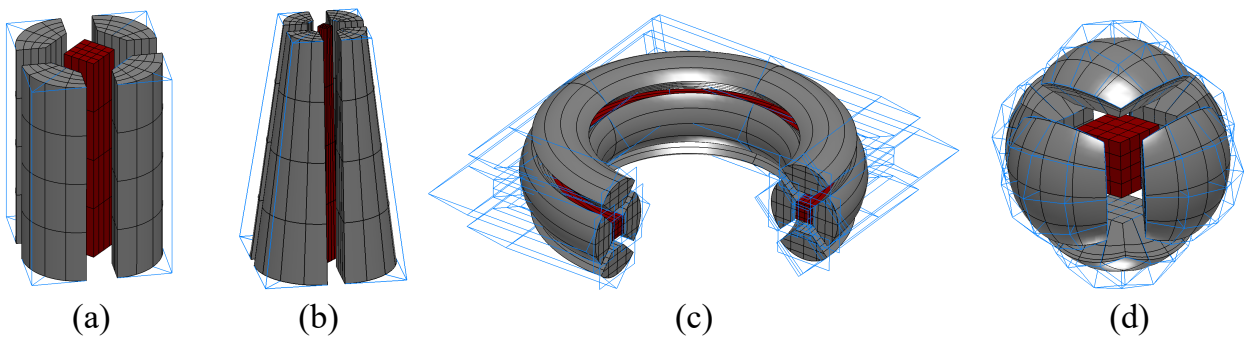

Figure 3: Non-singular primitives composed of trivariate B-splines: (a) A cylinder is composed by five extruded solids, whereas (b) a cone is composed of five ruled solids. (c) A torus is constructed using five solids of revolution, and (d) a sphere is composed of six ruled solids and one cuboid in its center.

2.4.2 V-model construction

A trivariate B-spline is limited to a cuboid topology. To represent general volumetric shapes, so-called 3-manifold V-cells ν_C^i are introduced which correspond to trimmed trivariate B-splines. V-cells occur due to the combination of the Boolean operations in the regions of overlapping. To this end, trivariate B-splines are trimmed at intersecting surfaces, and, depending on the Boolean operation, the intersection volume is then remodeled from the trimming surfaces using the Boolean constructor (see Fig. 4). A V-model V_m is composed of several V-cells, which are non-intersecting $\nu_C^i \cap \nu_C^j = \emptyset \ , \forall i \neq j$.

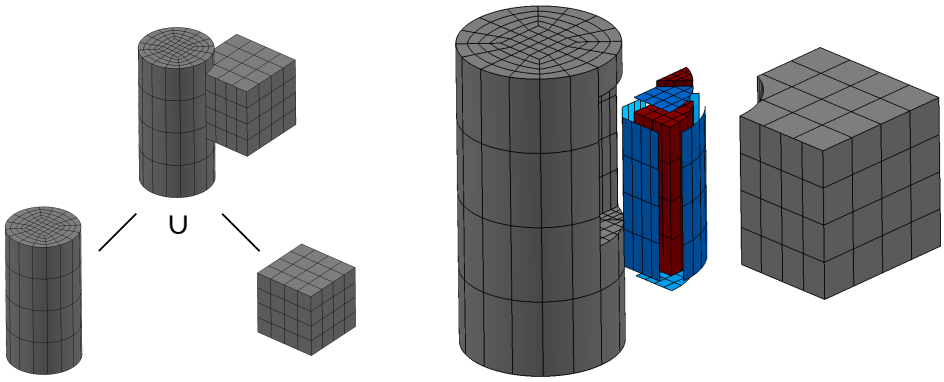

Figure 4: V-Model created as the union of a trivariate cuboid and a trivariate, non-singular cylinder. The intersected volume yields two V-cells (marked in red) which are constructed with the trimming surfaces (highlighted in blue).

V-cells store additional topological and adjacency information, which allows an efficient model inquiry. Adjacent V-cells share common trimming/boundary surfaces. Analogously to B-Rep, the boundary of the V-model ∂V_m forms a closed 2-manifold.

2.4.3 Point inclusion testing

In the context of the finite cell method, at first without considering functionally graded materials, the V-model only needs to provide a point inclusion test. To this end, an inverse mapping is carried out on each V-cell.

$$f : \boldsymbol{x} = \boldsymbol{\nu}_C^i(\boldsymbol{u}) \rightarrow \boldsymbol{u} \tag{4}$$

As splines can generally not be inverted analytically, the corresponding parameter position $\boldsymbol{u}$ must be determined iteratively using the Newton-Raphson algorithm. Yet, one should note that – since the splines are regular, i.e. the Jacobian never vanishes – a solution is always unique, if one exists. In the case $\boldsymbol{x} \cap \nu_C^i \neq \emptyset$ a parameter position can be found in the V-cell ν_C^i and the respective point $\boldsymbol{x}$ is inside the V-model. The duration of the inverse mapping can be substantially decreased providing a good guess as an initial value. This is exploited by the finite cell method as, due to the most frequent element- layer- and row-wise query, consecutive integration points are very often geometrically adjacent. Therefore, the last inner point on each V-cell is cached and used

as an initial guess for the next query.

3 Discussion and Results

3.1 Functionally graded material representation

The V-Rep framework provides two different ways to realize functionally graded materials: (a) the material properties can either be encoded directly into the volume of the V-cells (see Sec. 3.1.1) or (b) the FGM can be created in a constructive manner (see Sec. 3.1.2).

3.1.1 Functionally graded material inside the V-cells

As the smallest building blocks, the V-cells, are spline-based volumetric elements, it is natural to extend this spline description to also carry the material information.

V-Rep material representation Material properties such as Young's modulus, Poisson's ratio, thermal conductivity, density, etc. can easily be represented on the V-cells by simply extending the dimension of the control points $\mathbb{R}^{3+s}$, with $s > 0$ being the additional material parameters (see Eq. (3)). Consequently, evaluating the V-cell yields, in addition to the geometric coordinates, also the respective material values

$$\boldsymbol{V}^T = [x, y, z, m^1, ..., m^\sigma, ..., m^s] \in \mathbb{R}^{3+s} \,. \tag{5}$$

As an example, consider a control point that carries additional material properties for the Young's modulus E, Poisson's ratio ν, and thermal conductivity κ as needed for example 3.2.2: $\boldsymbol{P}^T_{i,j,k} = [x,\, y,\, z,\, E,\, \nu,\, \kappa]_{i,j,k}$.

The material properties of a V-cell, created from the overlap of two or more trivariate B-splines carrying different material information, require additional handling. Either one of the initial trivariate B-spline can be set prevailing and, thus, its properties are inherited to the V-cell, or the material properties are interpolated by some sort of blending scheme. For detailed information refer to [25].

Spline based material approximation Inside a patch, splines are typical of higher continuity, which renders them perfectly suitable for modeling smooth geometries. However, this restricts the material function to be of the same continuity. A remedy to also represent C^0 or discontinuous material distributions is given by knot-insertion, as the continuity depends on the multiplicity of the knots C^{p-m}, where p is the polynomial degree and m the number of multiple knots. Naturally, knot-insertion also reduces the potential continuity of the geometry. However, the original higher continuity is preserved in a geometrical sense. Hence, the model keeps its geometrical shape, whereas the material is allowed to have material kinks, or even to be discontinuous. Nevertheless, due to the global influence of the position and multiplicity of the knots, splines are not the method

of choice to represent highly discontinuous material distributions, as e.g. underlying voxel data provided by CT-scans.

Given a sufficiently smooth material distribution, the material 'coordinates' of the control points can be obtained using least-squares approximation (see Fig. 5). For each material property, the least-squares problem reads

$$\min_{\boldsymbol{\mu}^\sigma} \sum_{\lambda=1}^{n_{LS}} r_\lambda^2 = \min_{\boldsymbol{\mu}^\sigma} \|\boldsymbol{V}\left(\boldsymbol{u}_\lambda, \boldsymbol{\mu}^\sigma\right) - f_m^\sigma\left(\boldsymbol{x}_\lambda\right)\|_2^2 = \min_{\boldsymbol{\mu}^\sigma} \|\mathrm{A}(\boldsymbol{u}_\lambda)\boldsymbol{\mu}^\sigma - f_m^\sigma\left(\boldsymbol{x}_\lambda\right)\|_2^2 \,, \tag{6}$$

where n_{LS} is the number of sample points and $\boldsymbol{\mu}^\sigma = \mu_{i,j,k}^\sigma \in \mathbb{R}^{l\cdot n\cdot m}$ are the minimization variables (see Eq. (3) for l, m, n). The least squares problem is then solved for each material function f_m^σ and the respective material 'coordinate' $\boldsymbol{\mu}^\sigma$, $\sigma \in [1, s]$ of the control mesh $\boldsymbol{P}_{i,j,k} = \left[x, y, z, \mu^1, ..., \mu^\sigma, ..., \mu^s\right]_{i,j,k}^T$. Matrix $\mathrm{A} \in \mathbb{R}^{\nu\times(l\cdot n\cdot m)}$ contains the spline basis functions. The sample points are evaluated in the parameter space $\boldsymbol{u}_\lambda = [u, v, w]_\lambda^T \in \mathbb{R}^3$. Consequently, the material function needs to be evaluated in the same space (see Eq. (3))

$$f_m^\sigma\left(\boldsymbol{x}\right) = f_m^\sigma(\boldsymbol{V}(\boldsymbol{u}))\,. \tag{7}$$

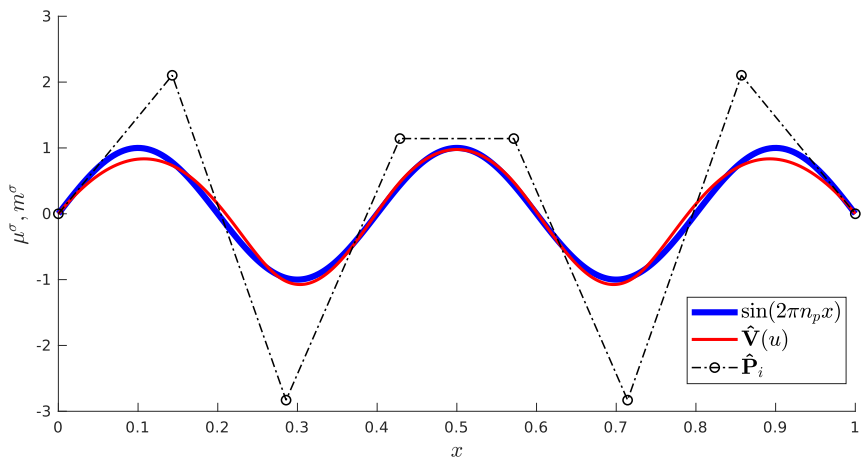

Figure 5: One-dimensional least squares approximation of a hypothetical sinusoidal material function $m^\sigma(x) = sin(2\pi n_p x)$, with $n_p = 2.5$ being the number of periods, yields the material 'coordinates' μ_i^σ. Note that the rather large deviation between the curves comes from the fact that the location (i.e. $x-$coordinate) of material control points is fixed.

3.1.2 Constructive functionally graded materials

A different kind of FGM are structures with changing material properties due to adaptions in the microstructure or density. A prominent example in nature is the trabecular bone, where the size and alignment of thin rods and plates of bone tissue create stiffness trajectories that follow the principal stresses for the most common load cases [72].

Today, additive manufacturing (AM) offers the possibility to create similarly complex structures. To this end, AM uses porous infill structures to support the outer hull. However, this infill is typically a repetitive lattice

and is either not taken into account for the load transfer, or it is assumed to be isotropic [73]. Nonetheless recent approaches in the field of topology optimization try to exploit the contribution of the infill to the load transfer [74]. Problem-fitted complex 3D anisotropic microstructures can reduce the printing time and material consumption substantially and at the same time improve the load-carrying properties and buckling behavior.

Gradually changing microstructure The V-Rep framework offers the possibility to create complex anisotropic microstructures with its tiling operation. Hereby, copies of a unit structure are consecutively created inside a base volume. Following the shape of the base volume and by using layers of different unit cells, a complex constructive FGM can be created. As the resulting microstructure is composed of several V-cells, it is again a V-model (see Fig. 6). Naturally, each V-cell can again represent a heterogeneous material distribution within its volume.

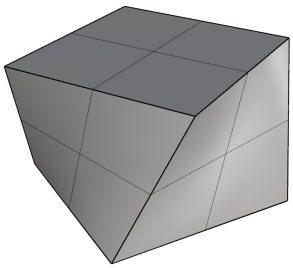

(a) Ruled base volume

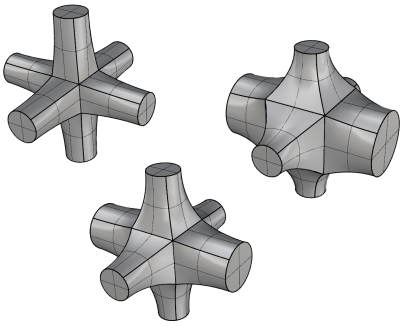

(b) Unit tiles

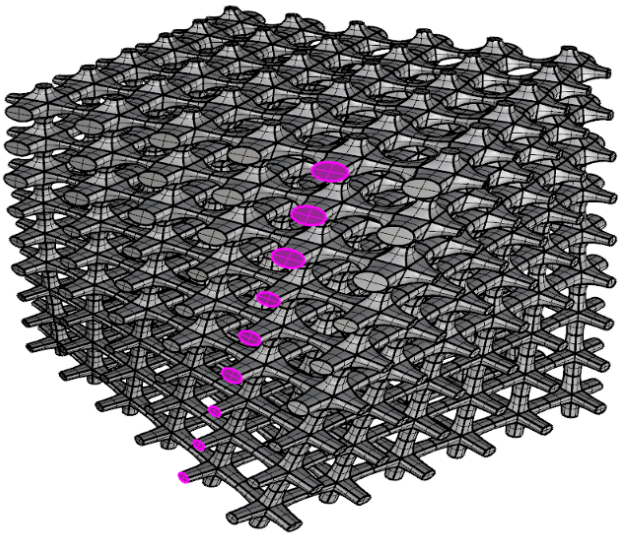

(c) microstructure

Figure 6: Functionally graded microstructure: (b) Three different anisotropic tiles, with a changing stiffer direction, are used to tile (a) a rotating ruled volume. (c) The entire resulting microstructure exhibits a continuously changing anisotropic stiffness.

Material characterization of unit tiles Detailed geometrical features of such microstructures require a fine numerical resolution to achieve reliable simulation results. To reduce the computational cost, a numerical homogenization can be used to evaluate a macroscopic mechanical behavior under specified loadings. The basic idea of this method is to approximate the solution of a macroscopic boundary value problem by solving less demanding microscopic problems [31]. This idea relies on the existence of a Representative Volume Element (RVE), which is a microstructural domain that is large enough to represent macroscopic behavior and small enough to ensure the scale separation. The mechanical quantities can then be transferred from micro- to macro-scale by using the Hill-Mandel condition, which is also called a 'macro-homogeneity condition'. This mean-

field numerical homogenization provides reliable estimates for the effective mechanical behavior if appropriate boundary conditions are chosen. In the case of periodic microstructures, such as the ones sketched in Tab. 2, periodic boundary conditions provide the best effective material properties. In order to generate a material database for these unit tiles, the numerical homogenization technique in combination with the Finite Cell Method [34] is used.

3.2 Numerical examples

To demonstrate the variety of simulatable functionally graded materials using a combination of V-reps and the FCM, five examples are presented. The first example serves as a verification of the method. To this end, a linear elastic simulation of a simple cuboid with a prescribed material distribution is performed. The second example, a coupled heat, thermo-elastic simulation of a curved thermal protection tile, underlines the applicability to examples of engineering relevance. The third example shows a simulation of a fully resolved constructive FGM in terms of a continuously changing microstructure. In the fourth example, the underlying tiles of the third example are evaluated in terms of a homogenization, which are then used in the fifth example to perform a simulation on a homogenized constructive FGM.

3.2.1 Example 1: Cuboid with sinusoidal material distribution

As a benchmark problem, the cuboid with varying material distribution in $z-$direction is chosen. The cuboid is a trivariate B-spline and is created with GuIrit [70]. As the spline basis functions are initially linear in each direction, they are not able to represent the material function $E(z)$. For this reason, a degree elevation to $r = 3$ and subsequent multiple knot insertions in $z-$direction were carried out, yielding a knot-vector of $W = [0, 0, 0, 0, 0.2, 0.4, 0.6, 0.8, 1, 1, 1, 1]$. The control points in $z-$direction are depicted in Fig. 7a. The cuboid has assigned a constant Poisson ratio of $\nu = 0.3$. The functionally graded Young's modulus is given as an analytical function

$$E(z) = 10^6 + 5 \cdot 10^4 \cdot sin(z\pi)\,. \tag{8}$$

The material 'coordinates' μ_i^E of the control points are computed using least squares with $n_{LS} = 100$ sample points, according to Eq. (6) (see Figs. 7b, and 8a)

$$\mu^E = [100000,\ 131438,\ 185772,\ 46415,\ 46415,\ 185772,\ 131438,\ 100000]\,. \tag{9}$$

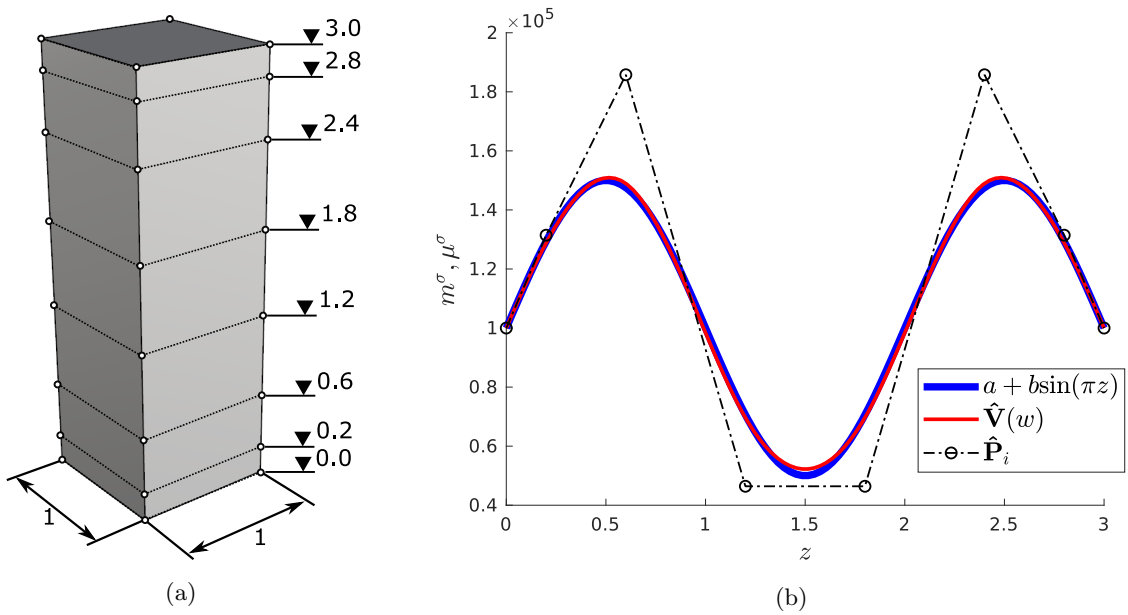

Figure 7: (a) Dimensions of the cuboid. (b) Least squares fitting of $E(z)$ yielding the material coordinates μ_i^E.

For the simulation, the cuboid is embedded into a slightly larger fictitious domain and discretized with $7 \times 7 \times 17$ finite cells. An octree with a maximum subdivision depth of $n = 4$ is used for the integration. Homogeneous Dirichlet boundary conditions are applied in $x-$direction on the left, in $y-$direction on the front, and in $z-$direction on the bottom surface using the penalty method. The cuboid is loaded on the top surface with a traction of $f = -1000$ in $z-$direction. A $p-$refinement is carried out to study the convergence behavior, increasing the order of the Legendre ansatz function from $p = 1...8$. The accuracy is measured by comparing the strain energy to a reference solution U_{ref}, which was computed with an extensive boundary-conforming finite element analysis (see Fig. 8b).

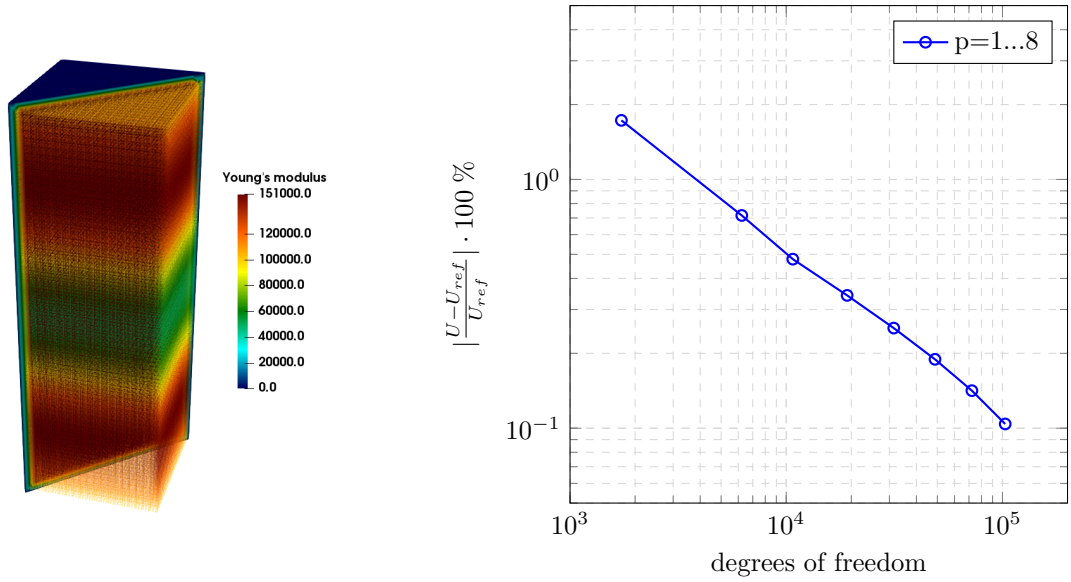

(a) (b)

Figure 8: (a) Young's modulus evaluated on integration points inside the cuboid and in the fictitious domain. (b) Relative error in the strain energy for polynomial degrees p = 1...8.

Fig. 9 shows the displacements and the von Mises stresses on the deformed cuboid. The regions of lower stiffness are undergoing a larger deformation. In the region of high stiffness, the stress concentrates on the surfaces.

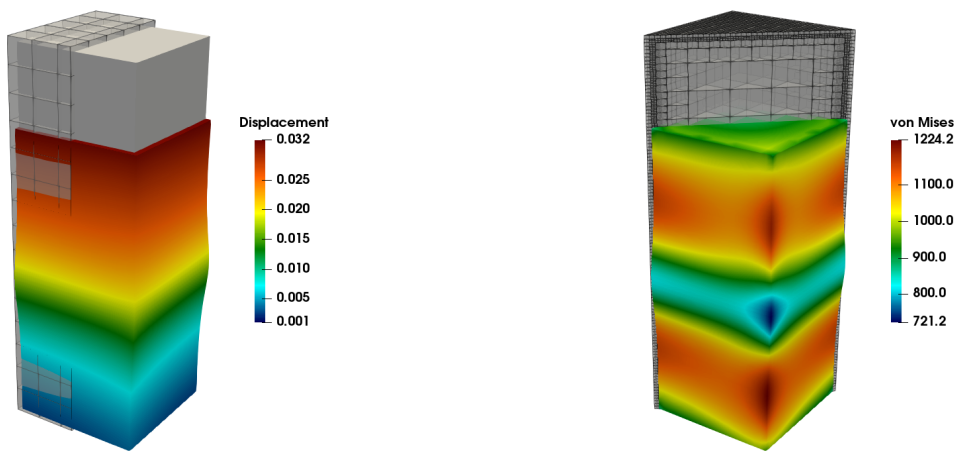

(a) (b)

Figure 9: (a) Displacements warped around the undeformed cuboid (grey block) embedded into the finite cell mesh. (b) Von Mises stresses and integration mesh. The deformation is scaled by a factor of 20.

3.2.2 Example 2: Curved thermal shielding tile

For the second example, three curved thermal shielding tiles are simulated. Such tiles are needed for high-temperature applications, such as re-entrance shielding for spacecrafts or the inner coating of fusion power plants. The tiles consist of a load-carrying zone made of titanium Ti and an insulating zone made of porous

silica SiO_2 with a porosity of 70%. Both materials have similar melting points of $\Theta_{Ti} = 1.668°C$ for titanium and $\Theta_{SiO_2} = 1.710°C$ for silica, which allows a fabrication with additive manufacturing using e.g. powder bed laser melting.

Special focus is laid on the continuity of the transition zone between these materials. The first discontinuous tile consists of two distinct domains where both domains are assumed to be homogeneous titanium and silica, respectively, i.e. there is no transition zone. The material is changed C^0-continuously in the second tile, and C^1-continuously in the third tile. To evaluate the stresses under a heat load, a coupled simulation is carried out. An initial thermal simulation provides the temperature distribution, which is then used to apply thermal strains for the subsequent thermo-elastic simulation. Consequently, the model will deform due to the different thermal expansion ratios. This deformation is, however, hindered by the different Young's moduli in the transition zone, then leading to internal stresses.

The underlying V-model consists of one V-cell and was generated by extruding a curved two-dimensional B-spline patch $5\,cm$ in $z-$direction. The V-cell has polynomial degrees of $p_x = p_y = 2$ in $x-$ and $y-$direction and $p_z = 1$ in $z-$direction. For the C^1- continuous tile, the polynomial degree in $z-$direction is $p_z = 2$. To construct the discontinuous tile, the V-model was split at $\Delta z_{div} = 1.25\,cm$ using knot-insertion. The knot vectors and $z-$coordinates of the control points for all tiles read as follows

$$U_{Discont.} = [0,\ 0,\ 0.25,\ 0.25,\ 1,\ 1] \tag{10}$$

$$U_{C^0} = [0,\ 0,\ 0.15,\ 0.35,\ 1,\ 1] \tag{11}$$

$$U_{C^1} = [0,\ 0,\ 0,\ 0.05,\ 0.29,\ 0.5,\ 1,\ 1,\ 1] \tag{12}$$

$$CP_{z,Discont.} = [0,\ 1.25,\ 1.25,\ 5] \tag{13}$$

$$CP_{z,C^0} = [0,\ 0.75,\ 1.75,\ 5] \tag{14}$$

$$CP_{z,C^1} = [0,\ 0.2,\ 0.8,\ 1.7,\ 3.6,\ 5]\,. \tag{15}$$

The resulting material distributions are depicted in Fig. 11 exemplary for the Young's modulus. The other material properties are distributed similarly. The parameters for the B-splines were chosen such that the integral of the material over the thickness is equal for all three tiles. Fig. 10 shows the outer dimensions of the tiles in cm.

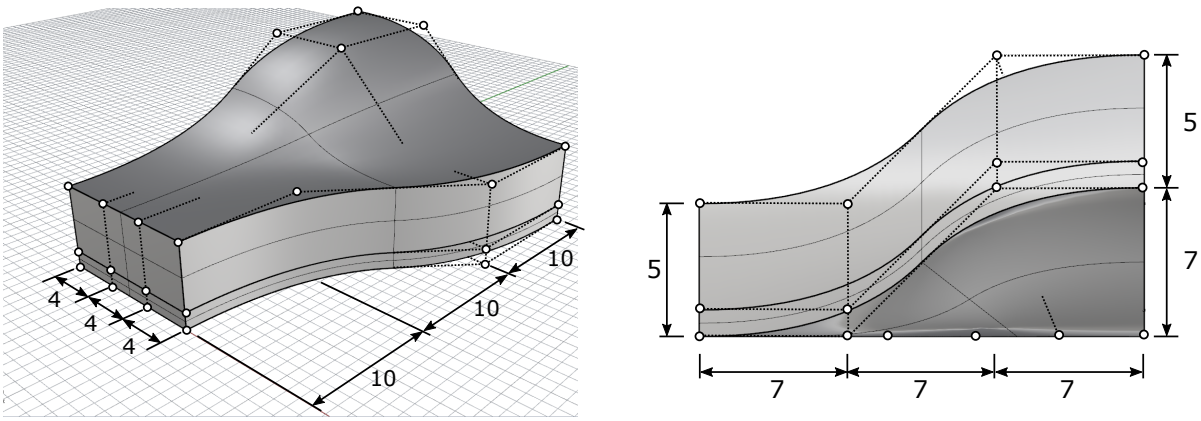

(a) (b)

Figure 10: Model dimensions (in cm) and control point mesh of the discontinuous tile in (a) isometric view, and (b) from the back side.

To perform the coupled simulation, four different material parameters are required for both materials (see Tab. 1). The properties were taken from AZO Materials and averaged if necessary [75]. Due to the porosity of the silica, the respective Young's modulus E_{SiO_2} and the thermal conductivity κ_{SiO_2} must be adapted. This is implemented based on the Gibson-Ashby criteria [76]. In contrast, the Poisson's ratio ν_{SiO_2} and the thermal expansions α_{SiO_2} require no adjustment [77].

Property	Symbol	Titanium	Silica (70% porosity)	Units
Young's Modulus	E	$11,600$	634	kN/cm^2
Poisson's Ratio	ν	0.36	0.17	–
Thermal conductivity	κ	0.216	$2.3 \cdot 10^{-3}$	W/cmK
Thermal expansion	α	$8.6 \cdot 10^{-6}$	$6.5 \cdot 10^{-7}$	$1/K$

Table 1: Material properties of titanium and porous silica for the coupled simulation.

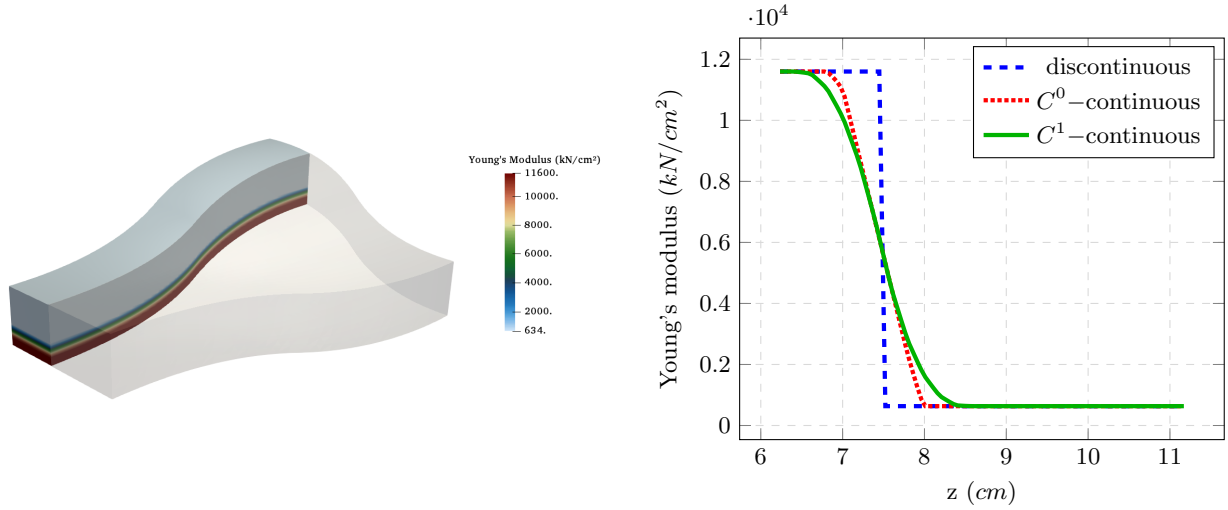

(a) (b)

Figure 11: Material distribution of the Young's modulus (a) inside the C^0-continuous tile and (b) plotted at $x = 5\,cm$, $y = 25\,cm$ over the thickness.

The simulation is based on $16 \times 23 \times 9$ finite cells with a polynomial degree of $p = 3$ and an integration subdivision depth of $n = 3$. For the preceding heat simulations, Dirichlet boundary conditions are applied with a prescribed heat of $1000°C$ on the top surface and $20°C$ on the bottom surface. The resulting temperature inside the tiles is then transferred as a body strain to perform a thermo-elastic simulation. Additionally, the tiles are clamped at the bottom surface. The simulation of the tile with the discontinuous material distribution is carried out on two separate meshes, which are 'glued' together in a weak sense along their coupling surface. To resolve the critical regions, the multi-level *hp*-method [60] is used to a refinement depth of two around the coupling surface for the meshes of the discontinuous tile and once in the transition zones of the continuous tiles (see Fig. 12).

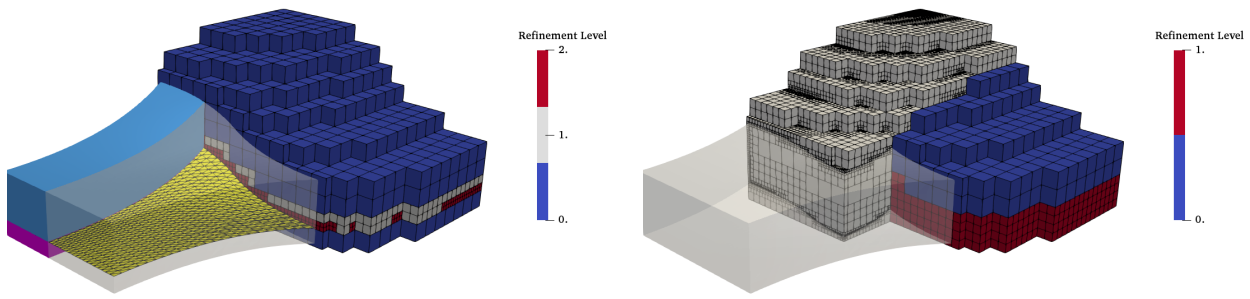

(a) (b)

Figure 12: Discretizations of (a) the discontinuous tile: The mesh is refined twice around the coupling surface (yellow), which divides the upper (light blue) and lower domain (purple). (b) The C^0-continuous tile: The FCM mesh is refined once in the transition zone (cells in blue are unrefined, and cells in red are refined once). The grey mesh in the background corresponds to the octree for the integration. The C^1-continuous tile is meshed and refined analogously.

To visualize the results inside the tiles, a cut through the model is investigated at $x = 5\,cm$. Fig. 13 shows the

temperature distribution and displacements of the C^0-continuous tile. The temperature and the displacement distributions are almost identical for all tiles. More relevant are the stress distributions. As can be seen in Fig. 14, a stress concentration occurs at the coupling surface of the discontinuous tile. Figs. 15 and 16 plot the temperature distribution, displacements, and stresses over the height at $x = 5\,cm$ and $y = 25\,cm$. The discontinuous material distribution yields a C^0-continuous heat and displacement distribution, which then entails a discontinuous stress distribution with a maximum peak at the interface region. This is critical as it will potentially cause delamination. The C^0-continuous material distribution, on the other hand, ensures a continuous and much smaller stress distribution throughout the entire domain. This effect can be augmented further by using a C^1-continuous material distribution. Continuous materials, on the other hand, involve a larger heat flux. For the 1D case, the thermal resistance is reduced to approximately 86% for the C^0-continuous and approximately 75% for the C^1-continuous material wirth respect to the discontinuous material distribution.

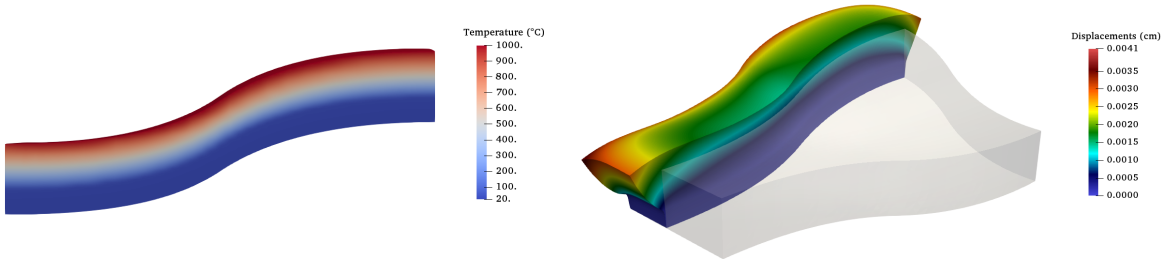

(a) (b)

Figure 13: C^0-continuous tile: (a) Temperature distribution and (b) displacements warped by a scaling factor of 1000.

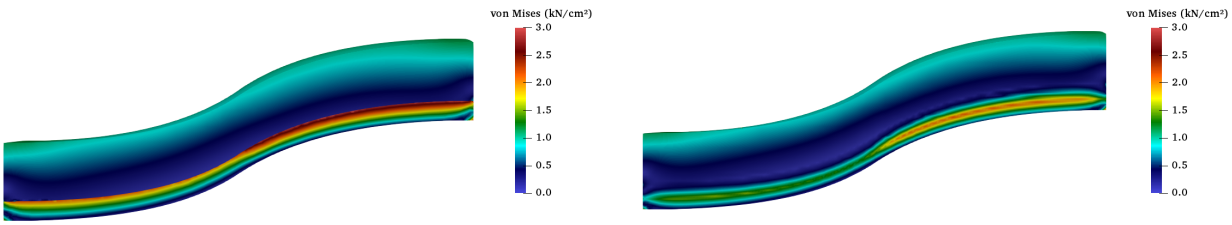

(a) (b)

Figure 14: Von Mises stresses of the (a) discontinuous and (b) C^0-continuous thermal shielding tile. The stress distribution of the C^1-continuous tile looks very similar to the C^0-continuous tile.

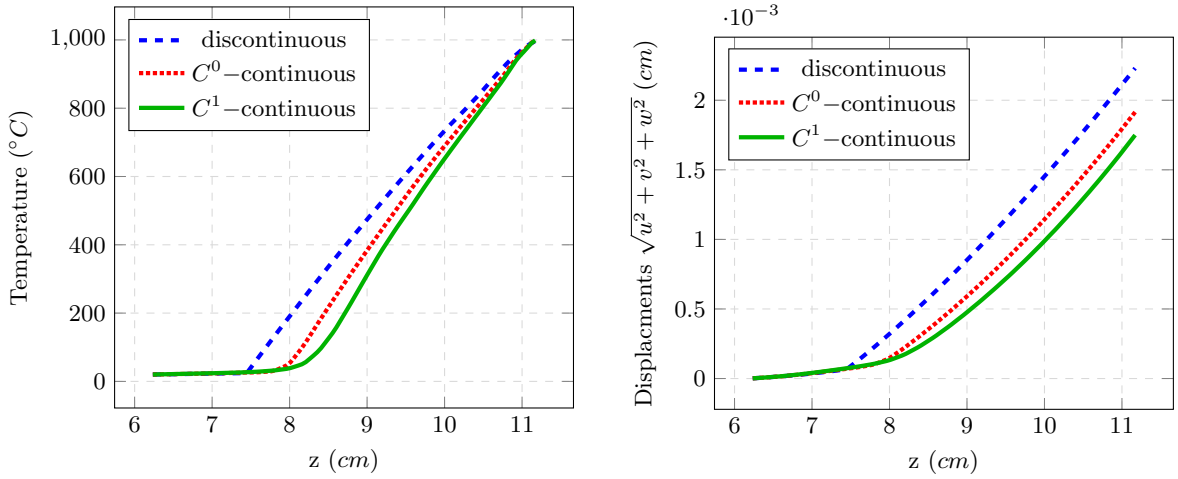

(a) (b)

Figure 15: Comparison of (a) the temperature and (b) the displacements of the discontinuous and continuous tiles at $x = 5\,cm$, $y = 25\,cm$ over the thickness.

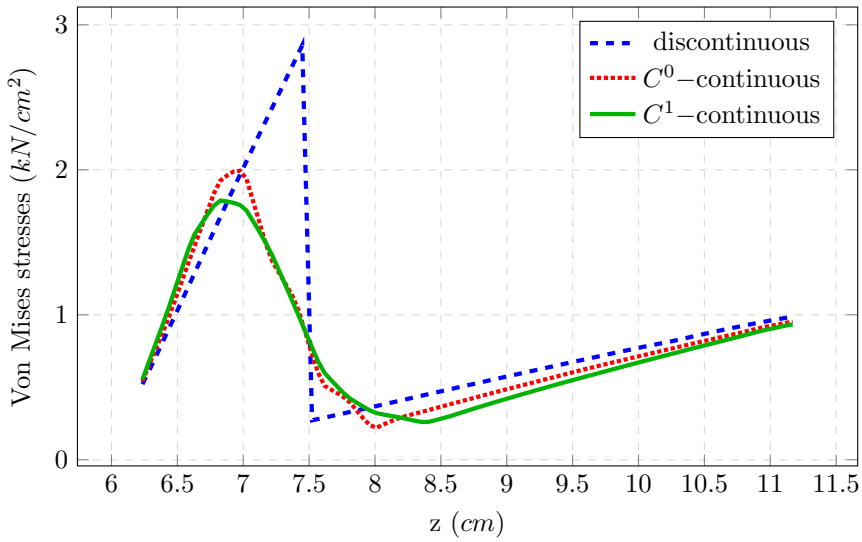

Figure 16: Comparison of the von Mises stresses of the discontinuous and continuous tiles at $x = 5\,cm$, $y = 25\,cm$ over the thickness.

3.2.3 Example 3: Anisotropic microstructure

For the third example, a linear-elastic simulation on the microstructure depicted in Figure 6 is carried out. It resembles a porous, foam-like microstructure stiffened by an outer shell. To generate this model, a continuously changing microstructure is created with GuIrit and converted into a surface model. The outer shell is added with a Boolean Union, and the microstructure outside to the shell is trimmed away. Finally, the computational model is extracted with a Boolean Intersection. Fig. 17 depicts the selection of the computational domain and the final model with the respective surfaces for the boundary conditions.

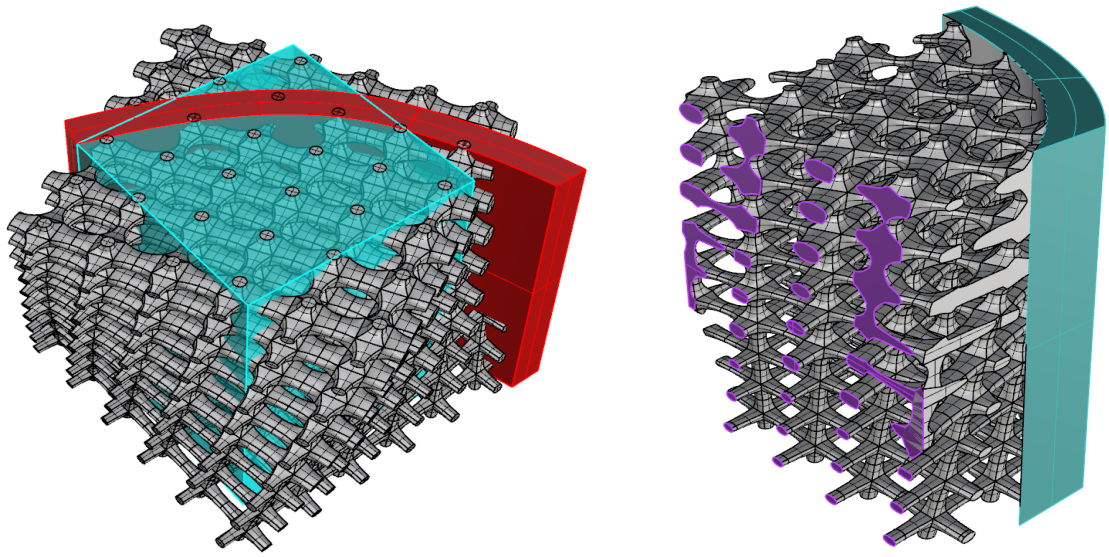

(a) (b)

Figure 17: (a) Selection of the computational domain (turquoise). An outer shell (red) is embedded into a microstructure. (b) Intersection of the microstructure with $\Omega_{\cup}$ leading to the physical domain Ω_{phy}. Boundary conditions are applied on the highlighted intersection surfaces.

The underlying microstructure consists of $6 \times 6 \times 9$ unit tiles and an overall number of 2268 trivariate B-splines. Converted into a surface model and after the deletion of internal surfaces, the microstructure consists of 8064 B-spline surfaces. For the simulation, homogeneous Dirichlet boundary conditions are applied on the cutting planes of the shell (see Fig. 17b – highlighted in turquoise). The top and bottom surface fix the displacements in $x-$ and $z-$direction, and the front and back surface restrict the displacements in $x-$ and $y-$direction. Dirichlet boundary conditions of $\Delta u = 0.1$ are applied on the outer surfaces on the left side (see Fig. 17b – highlighted in purple). All boundary conditions are enforced with the penalty method. The Young's modulus is $E = 100\,GPa$ and a Poisson's ratio of $\nu = 0.3\ \forall\, \boldsymbol{x} \in \Omega_{phy}$. The simulation is based on $20 \times 20 \times 20$ finite cells, employing Legendre polynomials of degree $p = 4$. The subdivision depth of the octree for the integration is set to $n = 4$.

Figs. 18 and 19 show the displacements and the von Mises stresses. Clearly, such a fully resolved simulation is slower than the numerical homogenization presented in section 3.1.2 – especially because homogenization in the linear case allows to create a lookup table. However, the discussed fully resolved model can be used to verify the homogenization. This is addressed in the following examples 3.2.4, and 3.2.5. Note, since the shape functions are bad suited to represent holes inside one finite cell, meaning 'material–void–material', the mircostructure needs to be resolved with many finite cells. A remedy can be local enrichment as presented in [78].

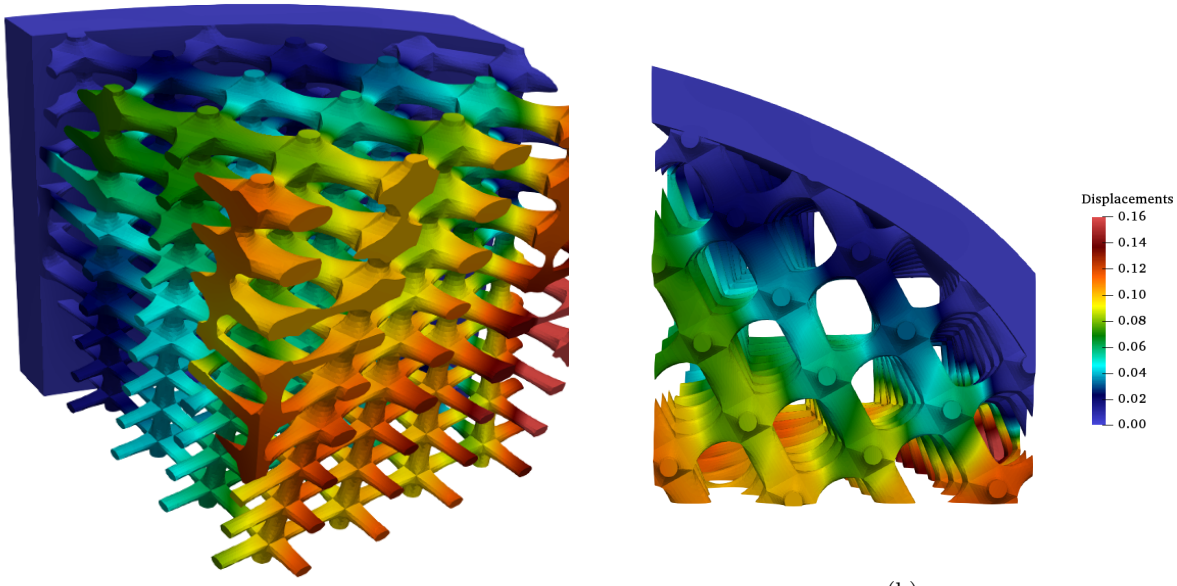

(a) (b)

Figure 18: Displacements in (a) isometric view and (b) from the top.

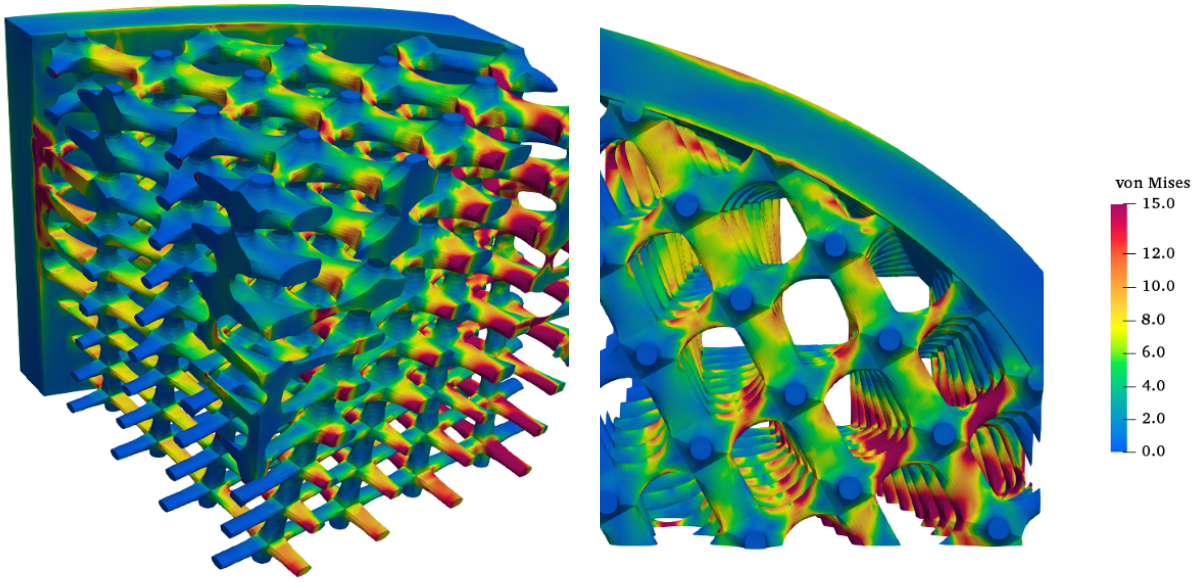

(a) (b)

Figure 19: Von Mises stresses in (a) isometric view and (b) from the top.

3.2.4 Example 4: Material characterization database for unit tiles

For a simulation of such microstructures (compare 3.2.3) with homogenized material, it is necessary to recover the material behavior of the RVEs, i.e., in this case, the unit tiles. To this end, homogenization simulations were carried out for all unit tiles. The material of the microstructure is considered to be steel with a Young's modulus of $E = 210\,GPa$ and a Poisson's ratio of $\nu = 0.3$. Each tile is discretized with $11 \times 11 \times 11$ finite cells

of polynomial degree $p = 5$. For the domain integration, the moment-fitting approach [62] with the depth of an underlying octree of $d = 6$ is chosen. As the structures under consideration are geometrically periodic, periodic boundary conditions are the natural choice for transferring the macroscopic quantities to the microscopic unit cells.

For arbitrary rotations, these constants can be computed analytically via a coordinate transformation. Then, the Bond-Transformation matrices [79] can be used to rotate the effective elasticity tensor by a matrix-matrix multiplication. Assume the following ordering of the macroscopic stresses σ_{ij}^M and strains ε_{ij}^M in the Voigt notation

$$\begin{bmatrix} \sigma_{11}^M \\ \sigma_{22}^M \\ \sigma_{33}^M \\ \sigma_{12}^M \\ \sigma_{23}^M \\ \sigma_{13}^M \end{bmatrix} = \begin{bmatrix} C_{11}^* & C_{12}^* & C_{13}^* & C_{14}^* & C_{15}^* & C_{16}^* \\ C_{12}^* & C_{22}^* & C_{23}^* & C_{24}^* & C_{25}^* & C_{26}^* \\ C_{13}^* & C_{23}^* & C_{33}^* & C_{34}^* & C_{35}^* & C_{36}^* \\ C_{14}^* & C_{24}^* & C_{34}^* & C_{44}^* & C_{45}^* & C_{46}^* \\ C_{15}^* & C_{25}^* & C_{35}^* & C_{45}^* & C_{55}^* & C_{56}^* \\ C_{16}^* & C_{26}^* & C_{36}^* & C_{46}^* & C_{56}^* & C_{66}^* \end{bmatrix} \begin{bmatrix} \varepsilon_{11}^M \\ \varepsilon_{22}^M \\ \varepsilon_{33}^M \\ \varepsilon_{12}^M \\ \varepsilon_{23}^M \\ \varepsilon_{13}^M \end{bmatrix} . \tag{16}$$

Then, the transformation of the effective elastic tensor reads as follows

$$\boldsymbol{C}' = \boldsymbol{M}\boldsymbol{C}^*\boldsymbol{N}^{-1} , \tag{17}$$

where $\boldsymbol{C}^*$ is the effective elasticity tensor, $\boldsymbol{C}'$ is the effective elasticity tensor in rotated coordinates, and $\boldsymbol{M}$ and $\boldsymbol{N}$ are the Bond-stress and the Bond-strain transformation matrices, respectively.

In this work, an exemplary a rotation of the unit tiles (see Fig. 6b) around the $z-$axis is considered. The Bond strain and stress matrices for this rotation are defined as follows:

$$M = \begin{bmatrix} cos^2(\alpha) & sin^2(\alpha) & 0 & sin(2\alpha) & 0 & 0 \\ sin^2(\alpha) & cos^2(\alpha) & 0 & -sin(2\alpha) & 0 & 0 \\ 0 & 0 & 1.0 & 0 & 0 & 0 \\ -\frac{sin(2\alpha)}{2} & \frac{sin(2\alpha)}{2} & 0 & cos(2\alpha) & 0 & 0 \\ 0 & 0 & 0 & 0 & cos(\alpha) & -sin(\alpha) \\ 0 & 0 & 0 & 0 & sin(\alpha) & cos(\alpha) \end{bmatrix} \tag{18}$$

$$N = \begin{bmatrix} cos^2(\alpha) & sin^2(\alpha) & 0 & \frac{sin(2\alpha)}{2} & 0 & 0 \\ sin^2(\alpha) & cos^2(\alpha) & 0 & -\frac{sin(2\alpha)}{2} & 0 & 0 \\ 0 & 0 & 1.0 & 0 & 0 & 0 \\ -sin(2\alpha) & sin(2\alpha) & 0 & cos(2\alpha) & 0 & 0 \\ 0 & 0 & 0 & 0 & cos(\alpha) & -sin(\alpha) \\ 0 & 0 & 0 & 0 & sin(\alpha) & cos(\alpha) \end{bmatrix} \tag{19}$$

Given a set of different (an-)isotropic unit tiles that can be used to construct such microstructures, it is possible to create a database of homogenized materials, which can then be used to simulate different macroscopic load cases. Furthermore – assuming that the macroscopic principal stresses were already computed on an isotropic material for a certain critical load case – this database can serve as a look-up table for selecting the best-suited unit tile for the respective region. Tab. 2 is a snippet of such a look-up table, and it shows the effective elasticity tensors for two varying material properties, i.e. the rotation around the $z-$axis and the diameter of the rod in $x-$direction. The material properties in-between can be interpolated. Of course, a complete look-up table would at least require rotations also around the $x-$ and $y-$axis and additional unit tiles with two stiffer directions, and equal stiffness in all three directions.

		Rotation around the $z-$axis		
		0°	22.5°	45°
Diameter of the rod in $x-$direction	$0.2\,mm$	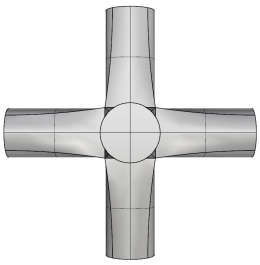 $C_{11} = 7.9\ GPa$ $C_{22} = 7.9\ GPa$	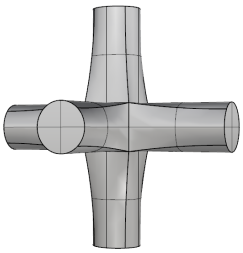 $C_{11} = 6.1\ GPa$ $C_{22} = 6.1\ GPa$	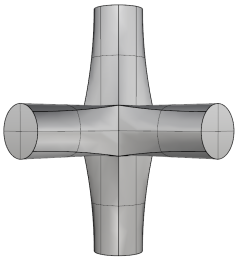 $C_{11} = 4.4\ GPa$ $C_{22} = 4.4\ GPa$
	$0.3\,mm$	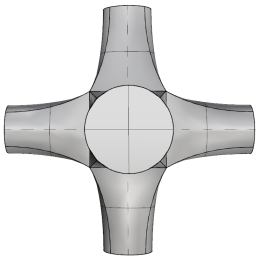 $C_{11} = 18.2\ GPa$ $C_{22} = 11.1\ GPa$	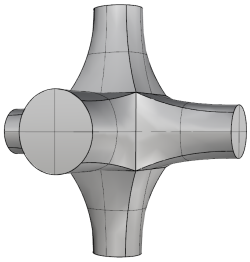 $C_{11} = 14.2\ GPa$ $C_{22} = 9.1\ GPa$	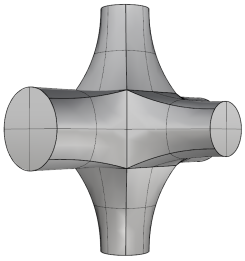 $C_{11} = 8.6\ GPa$ $C_{22} = 8.6\ GPa$
	$0.4\,mm$	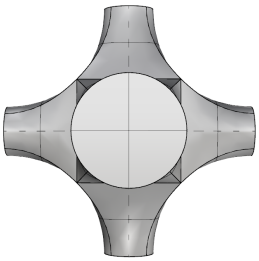 $C_{11} = 33.8\ GPa$ $C_{22} = 14.8\ GPa$	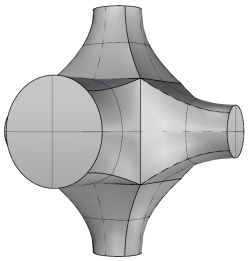 $C_{11} = 26.5\ GPa$ $C_{22} = 13.0\ GPa$	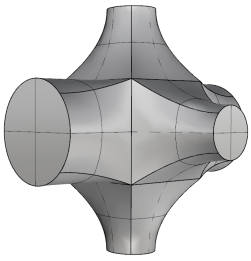 $C_{11} = 15.2\ GPa$ $C_{22} = 15.2\ GPa$

Table 2: Exemplary look-up table for the effective elasticity tensors (here represented by C_{11} and C_{22}) for changing diameters of the rod in $x-$direction and rotations around the $z-$axis.

Tile 1 (see Fig. 20) shows a cubic macroscopic material symmetry with three independent elasticity coeffi-

cients [80], namely C_{11}, C_{12} and C_{44}

$$C^*_{T1} = \begin{bmatrix} 7895.81 & 432.89 & 432.89 & 0.00 & 0.00 & 0.00 \\ 432.89 & 7895.81 & 432.89 & 0.00 & 0.00 & 0.00 \\ 432.89 & 432.89 & 7895.81 & 0.00 & 0.00 & 0.00 \\ 0.00 & 0.00 & 0.00 & 200.71 & 0.00 & 0.00 \\ 0.00 & 0.00 & 0.00 & 0.00 & 200.71 & 0.00 \\ 0.00 & 0.00 & 0.00 & 0.00 & 0.00 & 200.71 \end{bmatrix} \tag{20}$$

Due to the stiffer direction in $x-$direction, tile 2 and 3 (see Fig. 20) show a tetragonal effective material symmetry with $C_{11}, C_{22}, C_{44}, C_{55}, C_{12}$ and C_{23} as independent entries:

$$C^*_{T2} = \begin{bmatrix} 18246.81 & 1026.56 & 1026.56 & 0.00 & 0.00 & 0.00 \\ 1026.56 & 11066.80 & 659.81 & 0.00 & 0.00 & 0.00 \\ 1026.56 & 659.81 & 11066.80 & 0.00 & 0.00 & 0.00 \\ 0.00 & 0.00 & 0.00 & 769.49 & 0.00 & 0.00 \\ 0.00 & 0.00 & 0.00 & 0.00 & 590.69 & 0.00 \\ 0.00 & 0.00 & 0.00 & 0.00 & 0.00 & 769.49 \end{bmatrix} \tag{21}$$

$$C^*_{T3} = \begin{bmatrix} 33809.00 & 2037.73 & 2037.73 & 0.00 & 0.00 & 0.00 \\ 2037.73 & 14770.28 & 997.14 & 0.00 & 0.00 & 0.00 \\ 2037.73 & 997.14 & 14771.08 & 0.00 & 0.00 & 0.00 \\ 0.00 & 0.00 & 0.00 & 2022.10 & 0.00 & 0.00 \\ 0.00 & 0.00 & 0.00 & 0.00 & 1375.86 & 0.00 \\ 0.00 & 0.00 & 0.00 & 0.00 & 0.00 & 2022.17 \end{bmatrix} \tag{22}$$

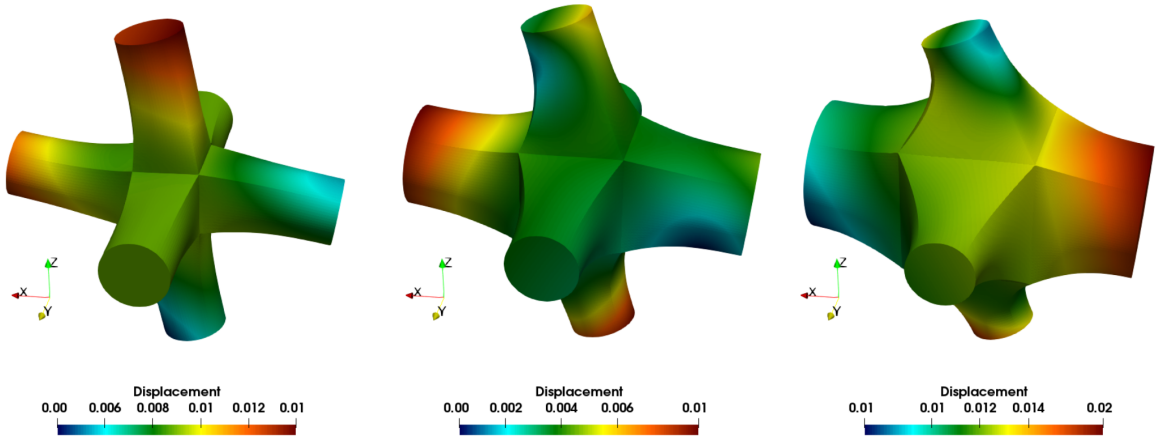

(a) Tile 1 (b) Tile 2 (c) Tile 3

Figure 20: Displacement field of the warped tiles with a scale factor $s = 10$.

Eq. (17) is used to obtain the effective material tensors for arbitrary rotations around the $z-$axis. For a rotational degree of 45°, the material constants are verified numerically (see Fig. 21).

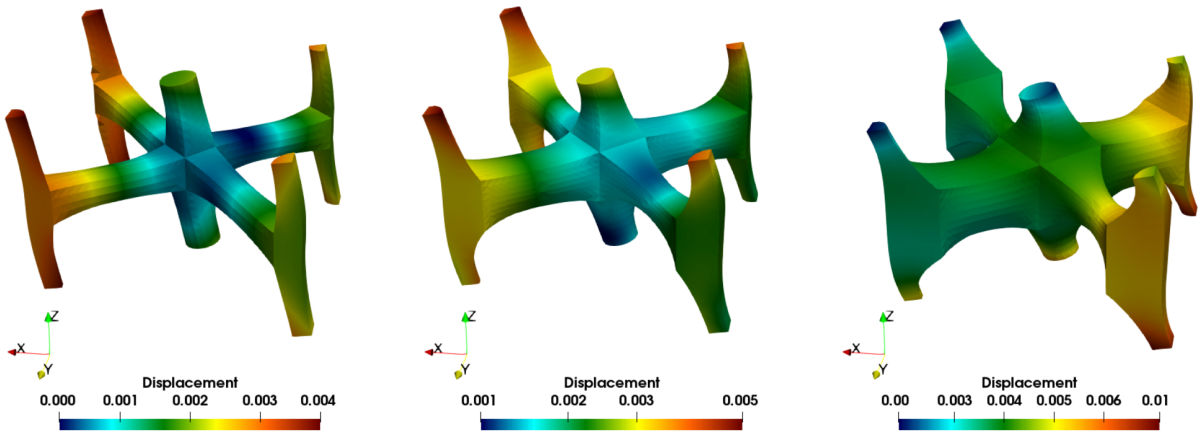

(a) Tile 1 (b) Tile 2 (c) Tile 3

Figure 21: Displacement field of the warped rotated tiles with a scale factor $s = 10$.

A rotation of tile 1 around the $z-$axis has no influence on the third, fifth, and sixth columns, neither on the respective rows of the effective tensor. The coefficient C_{11} equals C_{22} due to the geometrical symmetry in $x-$ and $y-$ directions. C_{14} and C_{24} are of equal magnitude but have opposite signs. Fig. 22 shows the remaining independent material constants with respect to the rotational angle. The results of the numerical simulation at 45° are marked with red crosses.

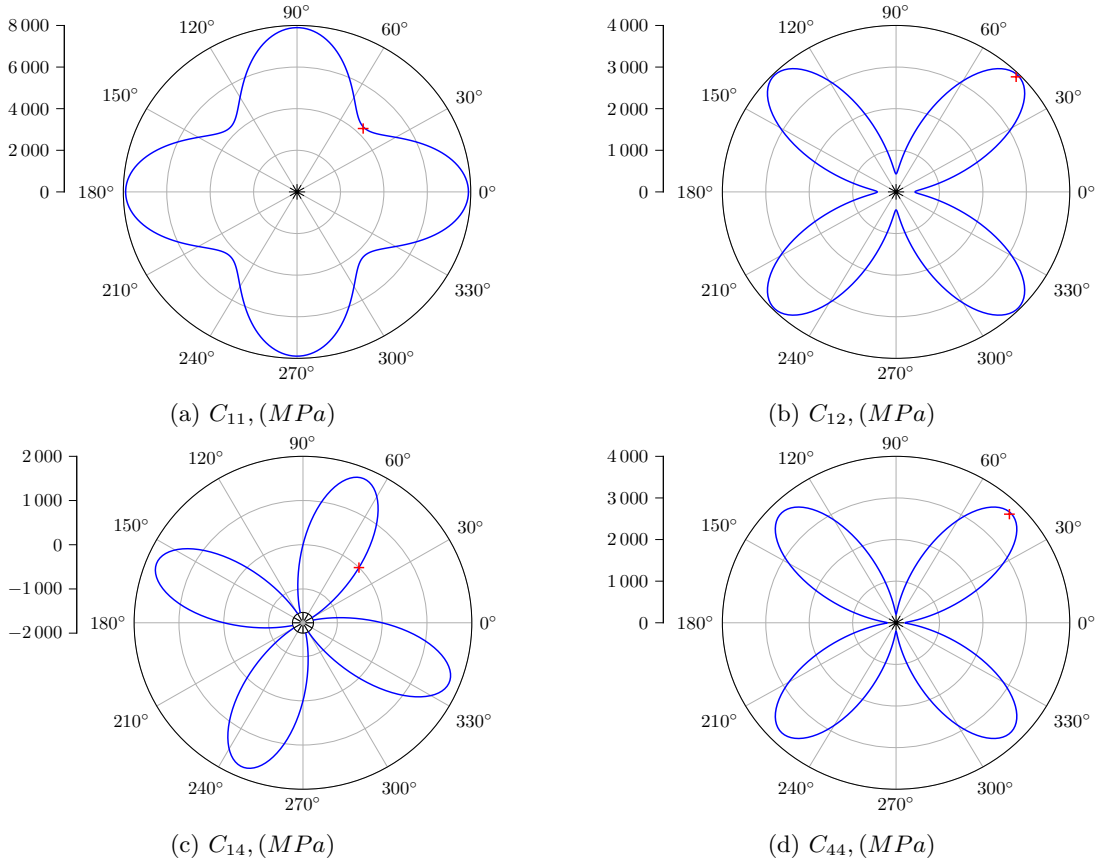

(a) $C_{11}, (MPa)$

(b) $C_{12}, (MPa)$

(c) $C_{14}, (MPa)$

(d) $C_{44}, (MPa)$

Figure 22: Independent elastic constants for tile 1 under rotation around the $z-$axis.

For tile 2, only the coefficient C_{33} which corresponds to the stiffness in $z-$direction remains unchanged under rotation around the $z-$axis. All other entries are affected by the altered symmetry. Considering a rotation angle of 90°, it is noteworthy that the coefficients C_{11} and C_{22} are switched with regard to the initial position. The same holds for the coefficient pairs $C_{55}-$ C_{66}, and C_{13}–C_{23}. The rest of the independent material parameters are depicted in Fig. 23. Again, the results of the numerical simulation at 45° are marked with red crosses.

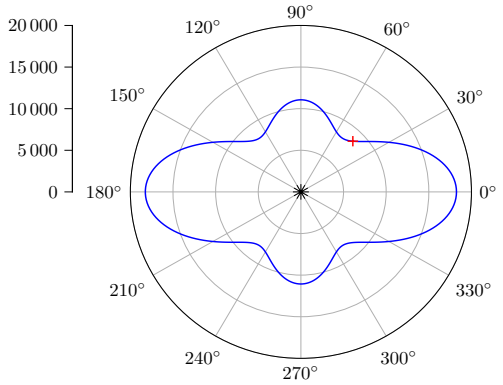

(a) $C_{11}, (MPa)$

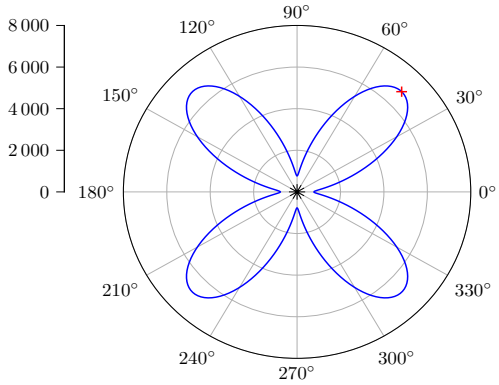

(b) $C_{44}, (MPa)$

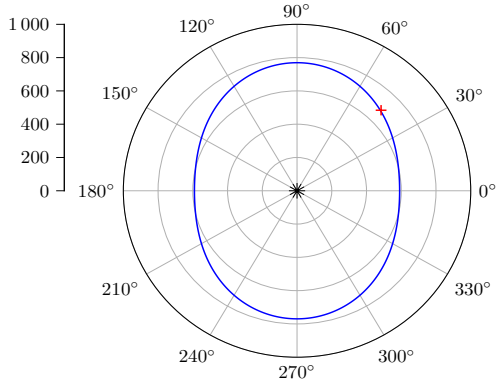

(c) $C_{55}, (MPa)$

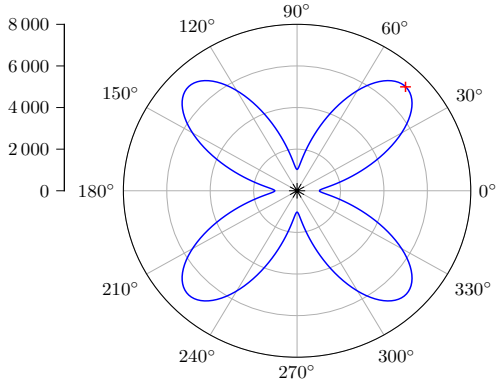

(d) $C_{12}, (MPa)$

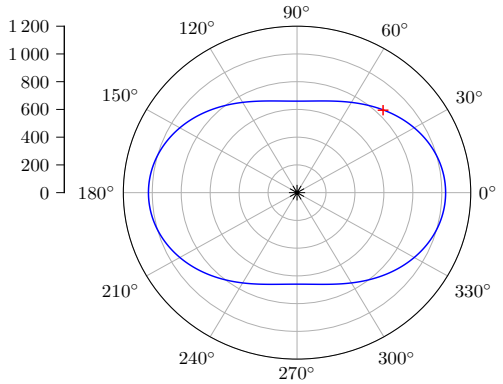

(e) $C_{13}, (MPa)$

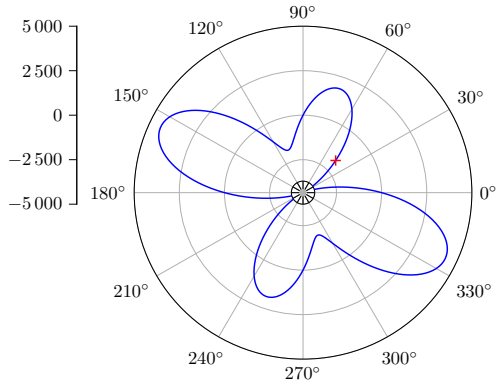

(f) $C_{14}, (MPa)$

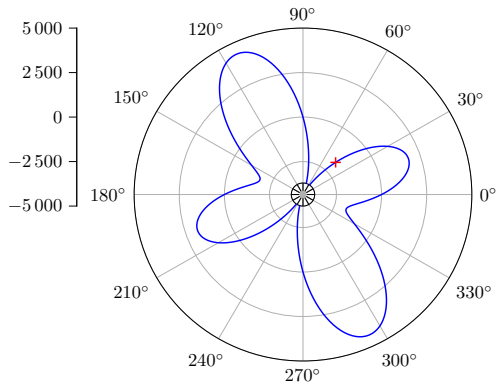

(g) $C_{24}, (MPa)$

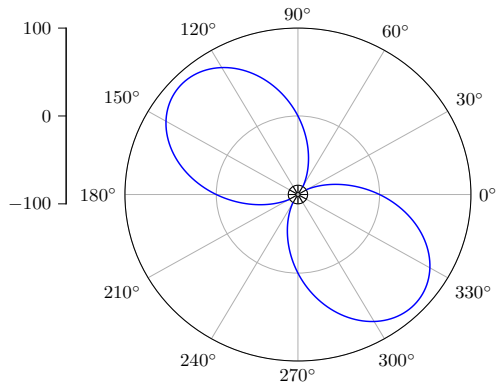

(h) $C_{56}, (MPa)$

Figure 23: Independent elastic constants for tile 2 under rotation around the $z-$axis.

Tile 3 exhibits similar material symmetries as the second tile. Fig. 24 shows the material coefficients. Again,

the results of the numerical simulation at 45° are marked with red crosses.

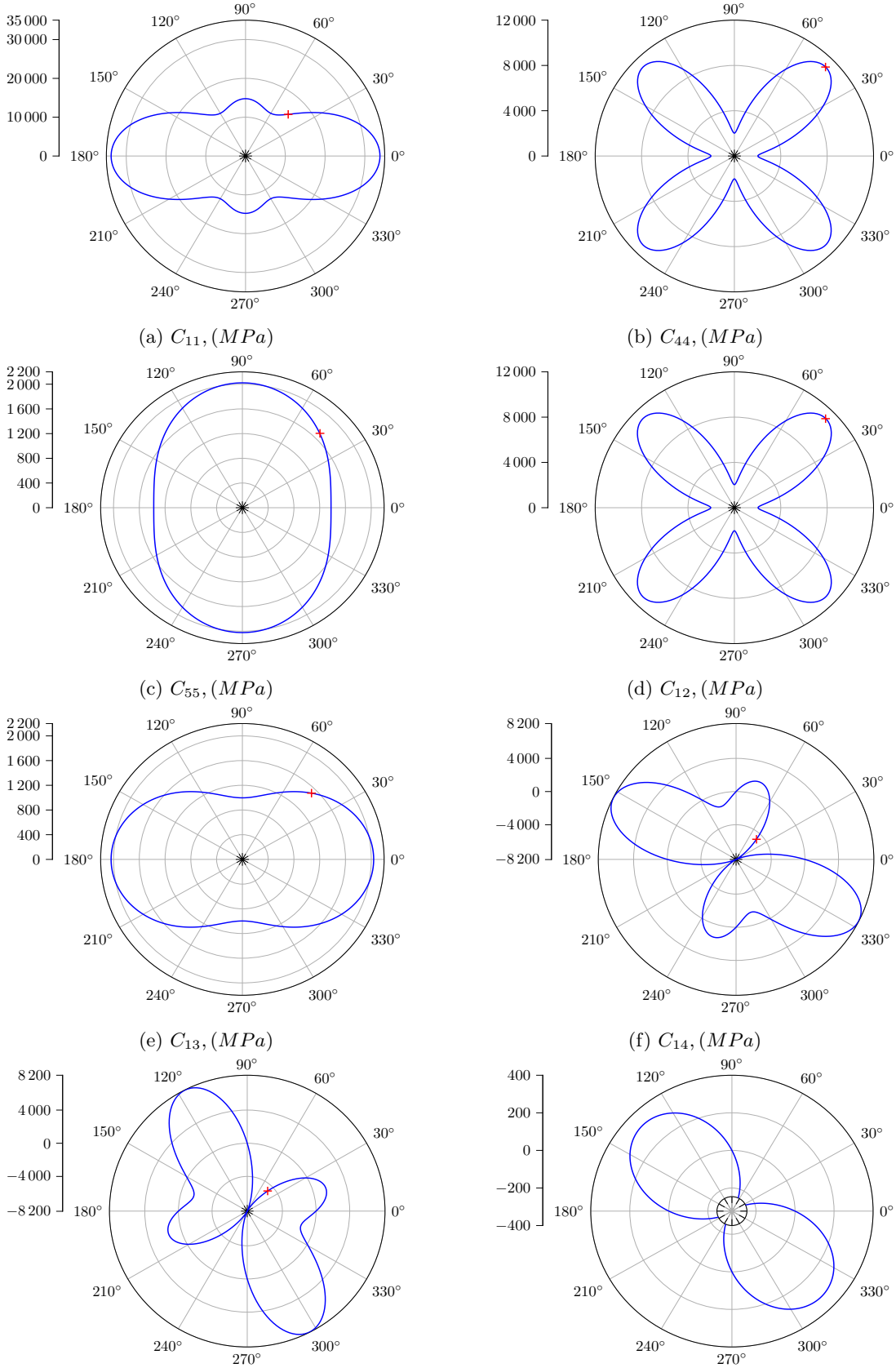

(a) $C_{11}, (MPa)$

(b) $C_{44}, (MPa)$

(c) $C_{55}, (MPa)$

(d) $C_{12}, (MPa)$

(e) $C_{13}, (MPa)$

(f) $C_{14}, (MPa)$

(g) $C_{24}, (MPa)$

(h) $C_{56}, (MPa)$

Figure 24: Independent elastic constants for tile 3 under rotation around the $z-$axis.

3.2.5 Example 5: Homogenized microstructure

Consider the model of Sec. 3.2.3 to be a part of a larger structure (see Fig. 25). Based on the material database for the homogenized unit tiles (see Tab. 2) it is possible to simulate such a large structure. For the simulation, the model is subdivided into an outer shell and an infill. The shell is considered to be of solid isotropic material, whereas the infill is a homogenized microstructure which continuously changes the two properties: a) the rotation angle ψ around the $z-$axis varies from $0°$ at the bottom to $90°$ at the top and b) the thickness of the rod $\emptyset$ increases from the center axis of the infill (in $z-$direction) $\emptyset = 0.2\,mm$ towards the interface of the shell $\emptyset = 0.4\,mm$. A uni-axial compression state is achieved by applying a uniform displacement of $\Delta z = -1.0$ on the top surface and restricting the displacements in $z-$direction on the bottom surface. Three additional point-bearings block the rigid body motions.

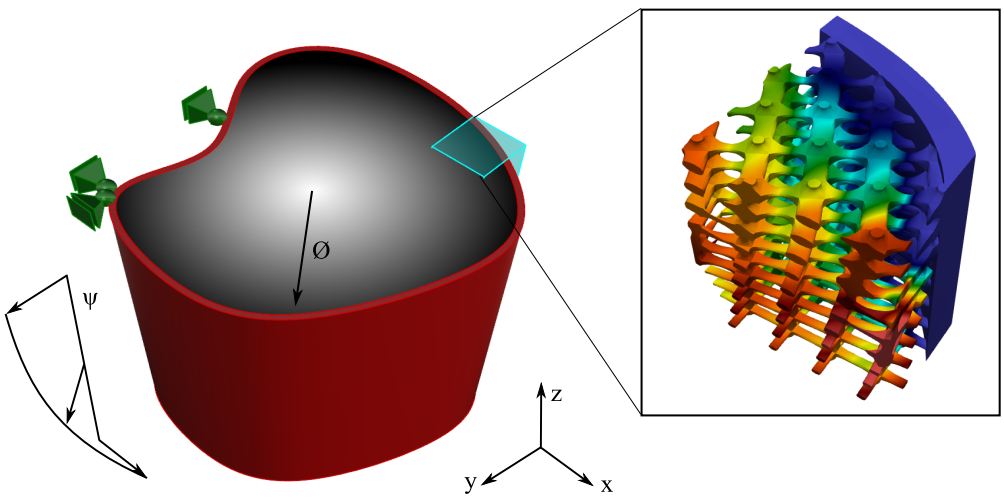

Figure 25: Structure consisting of a solid shell (red) and a homogenized microstructure (gray scale).

The simulation is based on $15 \times 15 \times 15$ high-order Legendre finite cells with a polynomial degree of $p = 4$, and moment-fitting with the depth of an underlying octree of $d = 4$ is chosen for the integration. At the interface between shell and infill, the mesh is refined to capture the material discontinuity. As the homogenization of the unit tiles was carried out with periodic boundary conditions, the behavior at the interface between shell and infill is not captured precisely. However, the affected domain is small compared to the overall structure, thus, the introduced error is negligible. If, however, the microscopic stress state at the transition from the micro-tiles to the shell is of interest, then a geometrically resolving simulation as in Sec. 3.2.3 can be performed.

A total of 13 independent material coefficients are required to evaluate the material tensor of the continuously changing microstructure. To this end, the material coefficients from the look-up table (see Tab. 2) are interpolated using spline fitting. Fig. 26 exemplary shows the interpolation for the material coefficients C_{11} and

C_{22}.

$$C = \begin{bmatrix} C_{11} & C_{12} & C_{13} & C_{14} & 0 & 0 \\ & C_{22} & C_{23} & C_{24} & 0 & 0 \\ & & C_{33} & C_{34} & 0 & 0 \\ & & & C_{44} & 0 & 0 \\ & & & & C_{55} & C_{56} \\ symm. & & & & & C_{66} \end{bmatrix} \tag{23}$$

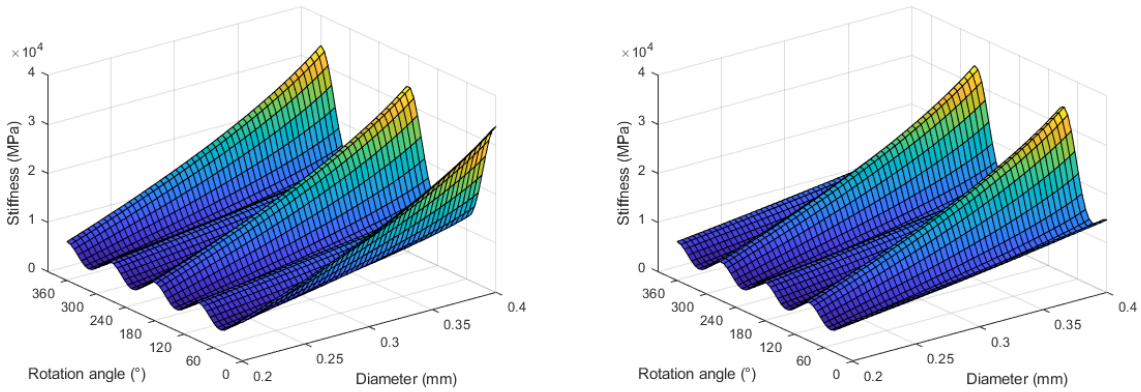

(a) C_{11} (b) C_{22}

Figure 26: Spline based interpolation of the material coefficients C_{11} and C_{22}.

Fig. 27 shows the displacements in $x-$direction and von Mises stresses of the structure under uni-axial compression $z-$direction. The load is mainly transferred through the stiffer shell, yet the contribution of the infill cannot be neglected. Due to the uni-axial compression, the rotation angle ψ of the microstructure has only little influence. The thickness of the rod Ø, on the other hand, can be deduced directly from the stress field of the infill.

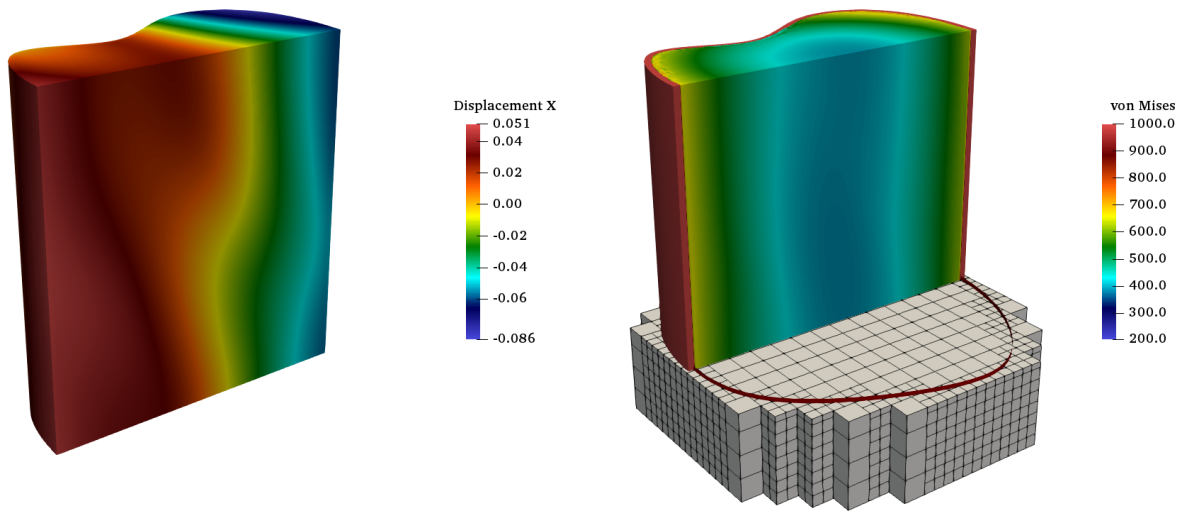

(a) (b)

Figure 27: (a) Displacements in $x-$direction and (b) von Mises stresses with the finite cell mesh.

It should be noted that a geometrical change has no influence on the overall workflow. Even a topological change does not lead to a re-meshing as would be required for a simulation with classical FEM or IGA. To illustrate such a topological change, a hole is drilled through the structure (see Fig. 28). In the context of the FCM, a cylinder is simply subtracted with the Boolean difference. As can be seen, the infill contributes less to the load transfer, and high stress concentrations appear at the walls of the hole.

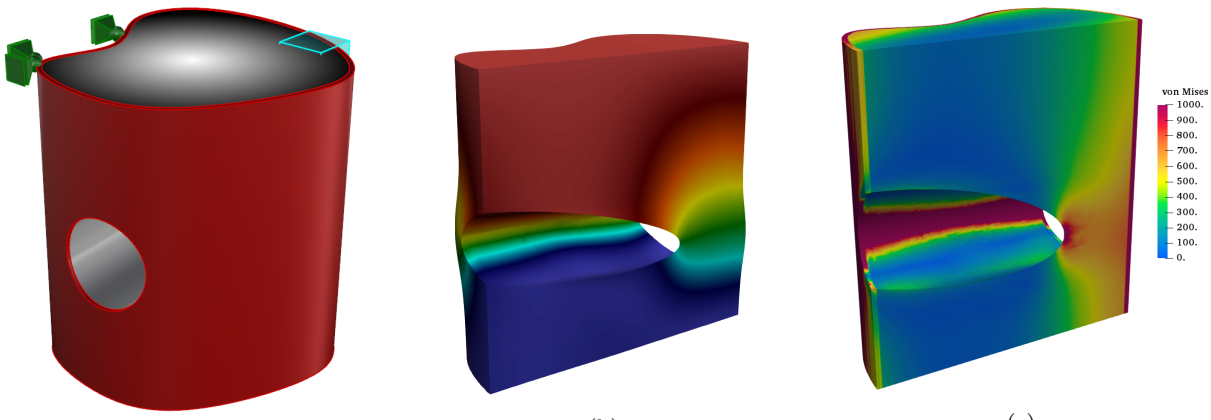

(a) (b) (c)

Figure 28: Structure with hole: (a) model, (b) displacements in $z-$direction (warped by a factor of $s = 2$), and (c) von Mises stresses.

4 Conclusions

In this work, we presented a methodology that allows to simulate functionally graded materials based on the V-rep framework and the FCM. V-reps, hereby, offer the possibility to apply the material directly to a model

or to design constructive FGM, such as microstructures. The Irit library and the graphical extension GuIrit provide a variety of volumetric modeling and analysis tools that can be utilized directly with the FCM. Although initially developed for IGA, FCM renders to be perfectly suited for the subsequent numerical simulation, as it is only reliant on the point inclusion test provided by the V-rep framework. Furthermore, FCM allows an adaptive non-global refinement towards critical regions, and it is perfectly suited for the homogenization of microstructures. Numerical examples proved the applicability to single-material as well as to multi-material FGM. Further developments could try to exploit the additive manufacturing tools of Irit, which allows to directly create G-code from the model. This could then be used in terms of numerical simulations of the additive manufacturing process.

5 Declarations

5.1 Availability of data and materials

The geometric models simulated and analysed during the current study are either reproducible with the provided information, or available from the corresponding author on reasonable request.

5.2 Competing interests

The authors declare that they have no competing interests.

5.3 Funding

We gratefully acknowledge the support of the German Research Foundation (DFG) under the Grant No. Ra 624/22-2. We would also like to thank the German Research Foundation (DFG) for its support through the TUM International Graduate School of Science and Engineering (IGSSE), GSC 81. Furthermore, we gratefully acknowledge the support of the Transregional Collaborative Research Centre SFB/TRR 277 "Additive Manufacturing in Construction. The Challenge of Large Scale", funded by the German Research Foundation (DFG).

5.4 Authors' contributions

BW was the corresponding author who wrote the main part of the paper, integrated the Irit geometry kernel into the Adhoc++ FCM framework, and carried out most of the simulations. NK wrote the part on homogenization and carried out the simulation and classification of the unit-tiles. SK was responsible for the content regarding the finite cell method and implementation issues. ER guided the general structure and contents of the paper, cross-checked the results and proposed most examples. GE provided the geometry kernel, and assistance for its access. Additionally, he was responsible for the content of the V-reps. All authors read and approved the final

manuscript.

5.5 Acknowledgements

We acknowledge the contributions of the research groups at the chair of Computation in Engineering regarding the development of the finite cell method framework *Adhoc++* and at the Center for Graphics and Geometric Computing concerning development of the geometry kernel *Irit* and CAD software *GuIrit*.

References

[1] S. Suresh, *Fundamentals of Functionally Graded Materials: Processing and Thermomechanical Behaviour of Graded Metals and Metal-Ceramic Composites.* London: IOM Communications Ltd, 1998. ISBN 978-1-86125-063-6 Open Library ID: OL3469177M.

[2] S. Bohidar, R. Sharma, and P. Mishra, "Functionally graded materials: A critical review," *Int J Res (IJR)*, vol. 1, pp. 289–301, Jan. 2014.

[3] N. Noda, "Thermal Stresses in Functionally Graded Materials," *Journal of Thermal Stresses*, vol. 22, no. 4-5, pp. 477–512, Jun. 1999. doi: 10.1080/014957399280841

[4] C. Zhang, F. Chen, Z. Huang, M. Jia, G. Chen, Y. Ye, Y. Lin, W. Liu, B. Chen, Q. Shen, L. Zhang, and E. J. Lavernia, "Additive manufacturing of functionally graded materials: A review," *Materials Science and Engineering: A*, vol. 764, p. 138209, Sep. 2019. doi: 10.1016/j.msea.2019.138209

[5] M. A. Meyers, J. McKittrick, and P.-Y. Chen, "Structural Biological Materials: Critical Mechanics-Materials Connections," *Science*, vol. 339, no. 6121, pp. 773–779, Feb. 2013. doi: 10.1126/science.1220854

[6] G. H. Paulino, E. Carlos, and N. Silva, "Topology Optimization Design Of Functionally Graded Structures," *Materials Science Forum*, vol. 492-493, Aug. 2005. doi: 10.4028/www.scientific.net/MSF.492-493.435

[7] L. Cheng, P. Zhang, E. Biyikli, J. Bai, J. Robbins, and A. To, "Efficient design optimization of variable-density cellular structures for additive manufacturing: Theory and experimental validation," *Rapid Prototyping Journal*, vol. 23, no. 4, pp. 660–677, Jun. 2017. doi: 10.1108/RPJ-04-2016-0069

[8] T. Liu, S. Guessasma, J. Zhu, W. Zhang, and S. Belhabib, "Functionally graded materials from topology optimisation and stereolithography," *European Polymer Journal*, vol. 108, pp. 199–211, Nov. 2018. doi: 10.1016/j.eurpolymj.2018.08.038

[9] M. Chmielewski and K. Pietrzak, "Metal-ceramic functionally graded materials - Manufacturing, characterization, application," *Bulletin of the Polish Academy of Sciences Technical Sciences*, vol. 64, Mar. 2016. doi: 10.1515/bpasts-2016-0017

[10] A. R. Studart, "Biological and Bioinspired Composites with Spatially Tunable Heterogeneous Architectures," *Advanced Functional Materials*, vol. 23, no. 36, pp. 4423–4436, 2013. doi: 10.1002/adfm.201300340

[11] K. Lee and H. Hee Yoo, "Temperature-Dependent Stress Analysis of Rotating Functionally Graded Material Gas Turbine Blade Considering Operating Temperature and Ceramic Particle Size," *Transactions of the Korean Society of Mechanical Engineers A*, vol. 38, Feb. 2014. doi: 10.3795/KSME-A.2014.38.2.193

[12] B. Zhang, P. Jaiswal, R. Rai, and S. Nelaturi, "Additive Manufacturing of Functionally Graded Material Objects: A Review," *Journal of Computing and Information Science in Engineering*, vol. 18, no. 4, p. 041002, Dec. 2018. doi: 10.1115/1.4039683

[13] F. Yan, W. Xiong, and E. Faierson, "Grain Structure Control of Additively Manufactured Metallic Materials," *Materials*, vol. 10, p. 1260, Nov. 2017. doi: 10.3390/ma10111260

[14] G. H. Loh, E. Pei, D. Harrison, and M. D. Monzón, "An overview of functionally graded additive manufacturing," *Additive Manufacturing*, vol. 23, pp. 34–44, Oct. 2018. doi: 10.1016/j.addma.2018.06.023

[15] A. O. Aremu, J. P. J. Brennan-Craddock, A. Panesar, I. A. Ashcroft, R. J. M. Hague, R. D. Wildman, and C. Tuck, "A voxel-based method of constructing and skinning conformal and functionally graded lattice structures suitable for additive manufacturing," *Additive Manufacturing*, vol. 13, pp. 1–13, Jan. 2017. doi: 10.1016/j.addma.2016.10.006

[16] T. D. Ngo, A. Kashani, G. Imbalzano, K. T. Q. Nguyen, and D. Hui, "Additive manufacturing (3D printing): A review of materials, methods, applications and challenges," *Composites Part B: Engineering*, vol. 143, pp. 172–196, Jun. 2018. doi: 10.1016/j.compositesb.2018.02.012

[17] A. Bandyopadhyay and B. Heer, "Additive manufacturing of multi-material structures," *Materials Science and Engineering: R: Reports*, vol. 129, pp. 1–16, Jul. 2018. doi: 10.1016/j.mser.2018.04.001

[18] J. Koopmann, J. Voigt, and T. Niendorf, "Additive Manufacturing of a Steel–Ceramic Multi-Material by Selective Laser Melting," *Metallurgical and Materials Transactions B*, vol. 50, no. 2, pp. 1042–1051, Apr. 2019. doi: 10.1007/s11663-019-01523-1

[19] E. Cohen, R. Riesenfeld, and G. Elber, *Geometric Modeling with Splines: An Introduction.* New York: A K Peters/CRC Press, Jul. 2001, vol. 1st Edition. ISBN 978-0-429-06428-9

[20] K.-H. Shin and D. Dutta, "Constructive Representation of Heterogeneous Objects," *Journal of Computing and Information Science in Engineering*, vol. 1, no. 3, pp. 205–217, Jun. 2001. doi: 10.1115/1.1403448

[21] X. Wu, W. Liu, and M. Y. Wang, "A CAD Modeling System for Heterogeneous Object," *Adv. Eng. Softw.*, vol. 39, no. 5, pp. 444–453, May 2008. doi: 10.1016/j.advengsoft.2007.03.002

[22] J. J. Shah and M. Mäntylä, *Parametric and Feature-Based CAD/CAM: Concepts, Techniques, and Applications.* John Wiley & Sons, 1995. ISBN 978-0-471-00214-7

[23] E. L. Doubrovski, E. Y. Tsai, D. Dikovsky, J. M. P. Geraedts, H. Herr, and N. Oxman, "Voxel-based fabrication through material property mapping: A design method for bitmap printing," *Computer-Aided Design*, vol. 60, pp. 3–13, Mar. 2015. doi: 10.1016/j.cad.2014.05.010

[24] V. Chandru, S. Manohar, and C. E. Prakash, "Voxel-based modeling for layered manufacturing," *IEEE Computer Graphics and Applications*, vol. 15, no. 6, pp. 42–47, Nov. 1995. doi: 10.1109/38.469516

[25] F. Massarwi and G. Elber, "A B-spline based framework for volumetric object modeling," *Computer-Aided Design*, vol. 78, pp. 36–47, Sep. 2016. doi: 10.1016/j.cad.2016.05.003

[26] T. J. R. Hughes, J. A. Cottrell, and Y. Bazilevs, "Isogeometric analysis: CAD, finite elements, NURBS, exact geometry and mesh refinement," *Computer Methods in Applied Mechanics and Engineering*, vol. 194, no. 39–41, pp. 4135–4195, Oct. 2005. doi: 10.1016/j.cma.2004.10.008

[27] E. Brivadis, A. Buffa, B. Wohlmuth, and L. Wunderlich, "Isogeometric Mortar methods," *Computer Methods in Applied Mechanics and Engineering*, vol. 284, Jul. 2014. doi: 10.1016/j.cma.2014.09.012

[28] B.-Q. Zuo, Z.-D. Huang, Y.-W. Wang, and Z.-J. Wu, "Isogeometric analysis for CSG models," *Computer Methods in Applied Mechanics and Engineering*, vol. 285, pp. 102–124, Mar. 2015. doi: 10.1016/j.cma.2014.10.046 00000.

[29] F. Fritzen, S. Forest, D. Kondo, and T. Böhlke, "Computational homogenization of porous materials of Green type," *Computational Mechanics*, vol. 52, no. 1, pp. 121–134, Jul. 2013. doi: 10.1007/s00466-012-0801-z

[30] D. Gross and T. Seelig, *Fracture Mechanics: With an Introduction to Micromechanics*, ser. Mechanical Engineering Series. Springer International Publishing, 2017. ISBN 978-3-319-71090-7

[31] S. Nemat-Nasser, M. Hori, and J. Achenbach, *Micromechanics: Overall Properties of Heterogeneous Materials*, ser. North-Holland Series in Applied Mathematics and Mechanics. Elsevier Science, 2013. ISBN 978-1-4832-9151-2

[32] D. H. Pahr, *Experimental and Numerical Investigations of Perforated FRP-Laminates.* VDI-Verlag, 2003. ISBN 978-3-18-328418-4

[33] E. Sanchez-Palencia and A. Zaoui, Eds., *Homogenization Techniques for Composite Media: Lectures Delivered at the CISM International Center for Mechanical Sciences, Udine, Italy, July 1-5, 1985*, ser. Lecture Notes in Physics. Berlin Heidelberg: Springer-Verlag, 1987. ISBN 978-3-540-47720-4

[34] N. Korshunova, J. Jomo, G. Lékó, D. Reznik, P. Balázs, and S. Kollmannsberger, "Image-based material characterization of complex microarchitectured additively manufactured structures," 2019. doi: https://arxiv.org/abs/1912.07415

[35] A. Düster, E. Rank, and B. A. Szabó, "The p-version of the finite element method and finite cell methods," in *Encyclopedia of Computational Mechanics*, E. Stein, R. Borst, and T. J. R. Hughes, Eds. Chichester, West Sussex: John Wiley & Sons, 2017, vol. 2, pp. 1–35. ISBN 978-1-119-00379-3

[36] E. Burman and P. Hansbo, "Fictitious domain finite element methods using cut elements: I. A stabilized Lagrange multiplier method," *Computer Methods in Applied Mechanics and Engineering*, vol. 199, no. 41-44, pp. 2680–2686, Oct. 2010. doi: 10.1016/j.cma.2010.05.011

[37] E. Heikkola, Y. Kuznetsov, K. Lipnikov, and Y. Kuznetsov, "Fictitious Domain Methods For The Numerical Solution Of Three-Dimensional Acoustic Scattering Problems," *Journal of Computational Acoustics*, May 1998.

[38] F. Auricchio, D. Boffi, L. Gastaldi, A. Lefieux, and A. Reali, "On a fictitious domain method with distributed Lagrange multiplier for interface problems," *Applied Numerical Mathematics*, vol. 95, pp. 36–50, Sep. 2015. doi: 10.1016/j.apnum.2014.05.013

[39] W. K. Liu, Y. Liu, D. Farrell, L. Zhang, X. S. Wang, Y. Fukui, N. Patankar, Y. Zhang, C. Bajaj, J. Lee, J. Hong, X. Chen, and H. Hsu, "Immersed finite element method and its applications to biological systems," *Computer Methods in Applied Mechanics and Engineering*, vol. 195, no. 13-16, pp. 1722–1749, Feb. 2006. doi: 10.1016/j.cma.2005.05.049

[40] R. Mittal and G. Iaccarino, "Immersed boundary methods," *Annu. Rev. Fluid Mech.*, vol. 37, pp. 239–261, 2005.

[41] E. Nadal, J. J. Ródenas, J. Albelda, M. Tur, J. E. Tarancón, and F. J. Fuenmayor, "Efficient Finite Element Methodology Based on Cartesian Grids: Application to Structural Shape Optimization," *Abstract and Applied Analysis*, vol. 2013, pp. 1–19, 2013. doi: 10.1155/2013/953786

[42] A. Düster, J. Parvizian, Z. Yang, and E. Rank, "The finite cell method for three-dimensional problems of solid mechanics," *Computer Methods in Applied Mechanics and Engineering*, vol. 197, no. 45–48, pp. 3768–3782, Aug. 2008. doi: 10.1016/j.cma.2008.02.036

[43] M. Joulaian, S. Duczek, U. Gabbert, and A. Düster, "Finite and spectral cell method for wave propagation in heterogeneous materials," *Computational Mechanics*, vol. 54, no. 3, pp. 661–675, Apr. 2014. doi: 10.1007/s00466-014-1019-z

[44] E. Rank, M. Ruess, S. Kollmannsberger, D. Schillinger, and A. Düster, "Geometric modeling, isogeometric analysis and the finite cell method," *Computer Methods in Applied Mechanics and Engineering*, vol. 249-252, pp. 104–115, Dec. 2012. doi: 10.1016/j.cma.2012.05.022

[45] J. P. Groen, M. Langelaar, O. Sigmund, and M. Ruess, "Higher-order multi-resolution topology optimization using the finite cell method," *International Journal for Numerical Methods in Engineering*, vol. 110, no. 10, pp. 903–920, Jun. 2017. doi: 10.1002/nme.5432

[46] S. Cai, W. Zhang, J. Zhu, and T. Gao, "Stress constrained shape and topology optimization with fixed mesh: A B-spline finite cell method combined with level set function," *Computer Methods in Applied Mechanics and Engineering*, vol. 278, pp. 361–387, Aug. 2014. doi: 10.1016/j.cma.2014.06.007

[47] M. Joulaian and A. Düster, "Local enrichment of the finite cell method for problems with material interfaces," *Computational Mechanics*, vol. 52, no. 4, pp. 741–762, Oct. 2013. doi: 10.1007/s00466-013-0853-8

[48] S. Duczek, M. Joulaian, A. Düster, and U. Gabbert, "Numerical analysis of Lamb waves using the finite and spectral cell methods," *International Journal for Numerical Methods in Engineering*, vol. 99, no. 1, pp. 26–53, Jul. 2014. doi: 10.1002/nme.4663

[49] A. Özcan, S. Kollmannsberger, J. Jomo, and E. Rank, "Residual stresses in metal deposition modeling: Discretizations of higher order," *Computers & Mathematics with Applications*, Nov. 2018. doi: 10.1016/j.camwa.2018.10.027

[50] T.-P. Fries and S. Omerović, "Higher-order accurate integration of implicit geometries," *International Journal for Numerical Methods in Engineering*, vol. 106, no. 5, pp. 323–371, May 2016. doi: 10.1002/nme.5121

[51] M. Joulaian, S. Hubrich, and A. Düster, "Numerical integration of discontinuities on arbitrary domains based on moment fitting," *Computational Mechanics*, vol. 57, no. 6, pp. 979–999, Jun. 2016. doi: 10.1007/s00466-016-1273-3

[52] B. Wassermann, S. Kollmannsberger, T. Bog, and E. Rank, "From geometric design to numerical analysis: A direct approach using the Finite Cell Method on Constructive Solid Geometry," *Computers & Mathematics with Applications*, Mar. 2017. doi: 10.1016/j.camwa.2017.01.027

[53] L. Nguyen, S. Stoter, T. Baum, J. Kirschke, M. Ruess, Z. Yosibash, and D. Schillinger, "Phase-field boundary conditions for the voxel finite cell method: Surface-free stress analysis of CT-based bone structures," *International Journal for Numerical Methods in Biomedical Engineering*, vol. 33, no. 12, p. e2880, 2017. doi: 10.1002/cnm.2880

[54] L. Kudela, S. Kollmannsberger, U. Almac, and E. Rank, "Direct structural analysis of domains defined by point clouds," *Computer Methods in Applied Mechanics and Engineering*, vol. 358, p. 112581, Jan. 2020. doi: 10.1016/j.cma.2019.112581

[55] B. Wassermann, S. Kollmannsberger, S. Yin, L. Kudela, and E. Rank, "Integrating CAD and numerical analysis: 'Dirty geometry' handling using the Finite Cell Method," *Computer Methods in Applied Mechanics and Engineering*, vol. 351, pp. 808–835, Jul. 2019. doi: 10.1016/j.cma.2019.04.017

[56] F. de Prenter, C. V. Verhoosel, G. J. van Zwieten, and E. H. van Brummelen, "Condition number analysis and preconditioning of the finite cell method," *Computer Methods in Applied Mechanics and Engineering*, vol. 316, no. Supplement C, pp. 297–327, Apr. 2017. doi: 10.1016/j.cma.2016.07.006

[57] M. Dauge, A. Düster, and E. Rank, "Theoretical and Numerical Investigation of the Finite Cell Method," *Journal of Scientific Computing*, vol. 65, no. 3, pp. 1039–1064, Mar. 2015. doi: 10.1007/s10915-015-9997-3

[58] F. de Prenter, "Preconditioned iterative solution techniques for immersed finite element methods: With applications in immersed isogeometric analysis for solid and fluid mechanics," Ph.D. dissertation, Eindhoven University of Technology, Eindhoven, Jun. 2019.

[59] D. Schillinger and E. Rank, "An unfitted hp-adaptive finite element method based on hierarchical B-splines for interface problems of complex geometry," *Computer Methods in Applied Mechanics and Engineering*, vol. 200, no. 47-48, pp. 3358–3380, Nov. 2011. doi: 10.1016/j.cma.2011.08.002

[60] N. Zander, T. Bog, M. Elhaddad, F. Frischmann, S. Kollmannsberger, and E. Rank, "The multi-level hp-method for three-dimensional problems: Dynamically changing high-order mesh refinement with arbitrary hanging nodes," *Computer Methods in Applied Mechanics and Engineering*, vol. 310, pp. 252–277, Oct. 2016. doi: 10.1016/j.cma.2016.07.007

[61] L. Kudela, N. Zander, S. Kollmannsberger, and E. Rank, "Smart octrees: Accurately integrating discontinuous functions in 3D," *Computer Methods in Applied Mechanics and Engineering*, vol. 306, pp. 406–426, Jul. 2016. doi: 10.1016/j.cma.2016.04.006

[62] S. Hubrich, P. D. Stolfo, L. Kudela, S. Kollmannsberger, E. Rank, A. Schröder, and A. Düster, "Numerical integration of discontinuous functions: Moment fitting and smart octree," *Computational Mechanics*, pp. 1–19, Jul. 2017. doi: 10.1007/s00466-017-1441-0

[63] A. Abedian, J. Parvizian, A. Düster, H. Khademyzadeh, and E. Rank, "Performance of Different Integration Schemes in Facing Discontinuities in the Finite Cell Method," *International Journal of Computational Methods*, vol. 10, no. 03, p. 1350002, Jun. 2013. doi: 10.1142/S0219876213500023

[64] S. Duczek and U. Gabbert, "Efficient integration method for fictitious domain approaches," *Computational Mechanics*, Aug. 2015. doi: 10.1007/s00466-015-1197-3

[65] S. Kollmannsberger, A. Özcan, J. Baiges, M. Ruess, E. Rank, and A. Reali, "Parameter-free, weak imposition of Dirichlet boundary conditions and coupling of trimmed and non-conforming patches," *Inter-*

national Journal for Numerical Methods in Engineering, vol. 101, no. 9, pp. 670–699, Mar. 2015. doi: 10.1002/nme.4817

[66] M. Ruess, Y. Bazilevs, D. Schillinger, N. Zander, and E. Rank, "Weakly enforced boundary conditions for the NURBS-based Finite Cell Method," in *European Congress on Computational Methods in Applied Sciences and Engineering (ECCOMAS)*, Vienna, Austria, 2012. ISBN 978-3-9502481-9-7

[67] M. Ruess, D. Schillinger, Y. Bazilevs, V. Varduhn, and E. Rank, "Weakly enforced essential boundary conditions for NURBS-embedded and trimmed NURBS geometries on the basis of the finite cell method," *International Journal for Numerical Methods in Engineering*, vol. 95, no. 10, pp. 811–846, Sep. 2013. doi: 10.1002/nme.4522

[68] Y. Guo and M. Ruess, "Nitsche's method for a coupling of isogeometric thin shells and blended shell structures," *Computer Methods in Applied Mechanics and Engineering*, vol. 284, pp. 881–905, Feb. 2015. doi: 10.1016/j.cma.2014.11.014

[69] T. Bog, N. Zander, S. Kollmannsberger, and E. Rank, "Weak imposition of frictionless contact constraints on automatically recovered high-order, embedded interfaces using the finite cell method," *Computational Mechanics*, vol. 61, no. 4, pp. 385–407, Apr. 2018. doi: 10.1007/s00466-017-1464-6

[70] G. Elber, "GUIRIT - Home Page," http://www.cs.technion.ac.il/~gershon/GuIrit/, Sep. 2019.

[71] G. Elber, Y.-J. Kim, and M.-S. Kim, "Volumetric Boolean sum," *Computer Aided Geometric Design*, vol. 29, no. 7, pp. 532–540, Oct. 2012. doi: 10.1016/j.cagd.2012.03.003

[72] D. Geraldes, "Orthotropic Modelling of the Skeletal System," Ph.D. dissertation, Imperial College of Science, Technology and Medicine, London, Mar. 2013.

[73] J. Jiang, X. Xu, and J. Stringer, "Support Structures for Additive Manufacturing: A Review," *Journal of Manufacturing and Materials Processing*, vol. 2, Sep. 2018. doi: 10.3390/jmmp2040064

[74] A. Clausen, N. Aage, and O. Sigmund, "Exploiting Additive Manufacturing Infill in Topology Optimization for Improved Buckling Load," *Engineering*, vol. 2, pp. 250–257, Jun. 2016. doi: 10.1016/J.ENG.2016.02.006

[75] A. Materials, "AZO Materials - Material Science - Materials Engineering - Home Page," https://www.azom.com/, Jan. 2020.

[76] W. Pabst, T. Uhlířová, E. Gregorová, and A. Wiegmann, "Young's modulus and thermal conductivity of closed-cell, open-cell and inverse ceramic foams – model-based predictions, cross-property predictions and numerical calculations," *Journal of the European Ceramic Society*, vol. 38, no. 6, pp. 2570–2578, Jun. 2018. doi: 10.1016/j.jeurceramsoc.2018.01.019

[77] W. Pabst and E. Gregorová, "Critical Assessment 18: Elastic and thermal properties of porous materials – rigorous bounds and cross-property relations," *Materials Science and Technology*, vol. 31, no. 15, pp. 1801–1808, Dec. 2015. doi: 10.1080/02670836.2015.1114697

[78] G. Legrain, N. Chevaugeon, and K. Dréau, "High order X-FEM and levelsets for complex microstructures: Uncoupling geometry and approximation," *Computer Methods in Applied Mechanics and Engineering*, vol. 241-244, pp. 172–189, Oct. 2012. doi: 10.1016/j.cma.2012.06.001

[79] W. L. Bond, "The Mathematics of the Physical Properties of Crystals," *Bell System Technical Journal*, vol. 22, no. 1, pp. 1–72, 1943. doi: 10.1002/j.1538-7305.1943.tb01304.x

[80] S. C. Cowin and S. B. Doty, "Modeling Material Symmetry," in *Tissue Mechanics*. New York, NY: Springer, 2007, pp. 139–167. ISBN 978-0-387-49985-7